BRNO UNIVERSITY OF TECHNOLOGY
VYSOKÉ UČENÍ TECHNICKÉ V BRNĚ

FACULTY OF MECHANICAL ENGINEERING
FAKULTA STROJNÍHO INŽENÝRSTVÍ

INSTITUTE OF PHYSICAL ENGINEERING
ÚSTAV FYZIKÁLNÍHO INŽENÝRSTVÍ

MAGNETIC PHASES IN AN ARTIFICIAL REALIZATION OF THE SQUARE ICE MODEL
MAGNETICKÉ FÁZE UMĚLÉHO SPINOVÉHO LEDU NA ČTVERCOVÉ MŘÍŽCE

MASTER'S THESIS
DIPLOMOVÁ PRÁCE

AUTHOR — **Bc. Ondřej Brunn**
AUTOR PRÁCE

SUPERVISOR — **Nicolas Rougemaille**
VEDOUCÍ PRÁCE

BRNO 2019

VYSOKÉ UČENÍ TECHNICKÉ V BRNĚ
FAKULTA STROJNÍHO INŽENÝRSTVÍ

Zadání diplomové práce

Ústav:	Ústav fyzikálního inženýrství
Student:	**Bc. Ondřej Brunn**
Studijní program:	Aplikované vědy v inženýrství
Studijní obor:	Fyzikální inženýrství a nanotechnologie
Vedoucí práce:	**Nicolas Rougemaille**
Akademický rok:	2018/19

Ředitel ústavu Vám v souladu se zákonem č.111/1998 o vysokých školách a se Studijním a zkušebním řádem VUT v Brně určuje následující téma diplomové práce:

Magnetické fáze umělého spinového ledu na čtvercové mřížce

Stručná charakteristika problematiky úkolu:

Umělé systémy se ve fyzice často používají k tomu, aby bylo možné vytvořit, prozkoumat a manipulovat se zajímavými vlastnostmi hmoty, které v přírodě neexistují nebo které může být náročné zkoumat jinak. V magnetismu pevných látek byly zavedeny umělé soustavy interagujících nanomagnetů jako možný způsob, jak experimentálně vyrobit různé typy frustrovaných spinových modelů. Tyto magnetické systémy umožňují vizualizovat nekonvenční magnetické fáze a exotické kolektivní jevy přímo v reálném prostoru.
Tato diplomová práce se zaměřuje na zkoumání exotické nízkoenergetické fyziky čtvercového modelu ledu v umělých polích magnetických nanostruktur. Konkrétně se projekt snaží ukázat, že skenování fázovým diagramem modelu čtvercového ledu může být dosaženo experimentálně za předpokladu, že umělá pole jsou navržena vhodným způsobem.
Tato pole budou vyrobena za použití elektronové litografie a po demagnetizaci (buď pomocí magnetického pole nebo tepelného žíhání) budou zkoumána pomocí MFM. Výsledné magnetické konfigurace budou porovnány s teoretickými předpovědami pomocí analýzy párových spinových korelací.

Cíle diplomové práce:

1) Ukažte, že symetrický bod modelu čtvercového ledu lze nalézt experimentálně a lze pozorovat známky algebraické coulombovské kapaliny.
2) Ukažte, že magnetické kvazičástice (magnetické monopóly) mohou být zachyceny ve spinovém ledu a zkoumejte jejich relaxační dynamiku.
3) Určete, zda může být hustota těchto magnetických kvazičástic měněna dle potřeby a je tedy možné otestovat teorii rozpadu spinu zavedenou před několika lety.

Seznam doporučené literatury:

NISOLI, C., MOESSNER, R. and SCHIFFER, P., Artificial spin ice: Designing and imaging magnetic frustration. Reviews of Modern Physics 85, 1473 (2013).

WANG, R. F., et al., artificial ‘spin ice’ in a geometrically frustrated lattice of nanoscale ferromagnetic islands. Nature 439, 303 (2006).

PERRIN, Y., CANALS, B. and ROUGEMAILLE, N., Extensive degeneracy, Coulomb phase and magnetic monopoles in artificial square ice. Nature 540, 410 (2016).

CANALS, B., CHIOAR, I.-A., et al., Fragmentation of magnetism in artificial kagome dipolar spin ice. Nature Communications 7, 11446 (2016).

BROOKS-BARTLETT, M. E. et al., Magnetic-Moment Fragmentation and Monopole Crystallization. Physical Review X 4, 011007 (2014).

Termín odevzdání diplomové práce je stanoven časovým plánem akademického roku 2018/19

V Brně, dne

L. S.

prof. RNDr. Tomáš Šikola, CSc. ředitel ústavu	doc. Ing. Jaroslav Katolický, Ph.D. děkan fakulty

ABSTRACT

Artificial spin systems are convenient tool for exploring and manipulating unconventional exotic low-energy states directly in real space. Experimental realization of these system is made by pattering arrays of interacting nanomagnets with given geometry. First and also probably the most extensively studied artificial system have regular square lattice. In this work we deal with the modification of the square geometry that enable us to induce distinct magnetic phases of ice-type models. Results show that with appropriate tuning of the modification, several magnetic phases can be reached, including the disordered spin-liquid phase with trapped magnetic quasi-particles (magnetic monopoles).

KEYWORDS

Artificial spin ice, artificial magnetic spin systems, square lattice, magnetic phases, ice-type model, vertex model, magnetic force microscopy.

ABSTRAKT

Umělé spinové systémy jsou vhodným nástrojem pro zkoumání a ovlivňování neobvyklých exotických nízko-energiových stavů přímo v reálném prostoru. Experimentální realizace těchto systémů jsou založeny na výrobě vzájemně interagujících nano-magnetů uspořádaných do požadované geometrie. Prvním a asi i nejvíce studovaným umělým systémem je prostá čtvercová mřížka. V této práci se zabýváme modifikováním této čtvercové geometrie, které umožní zachycení různých magnetických fází založených na modelech ledu. Výsledky ukazují, že vhodným nastaveném této modifikace lze realizovat různé magnetické fáze, včetně neuspořádané spinové kapalné fáze s uvězněnými magnetickými kvazičásticemi (magnetickými monopóly).

KLÍČOVÁ SLOVA

Umělé systémy spinového ledu, umělé magnetické spinové systémy, čtvercová mřížka, magnetické fáze, model ledu, vertex modely, mikroskopie magnetických sil.

BRUNN, O. *Magnetic phases in an artificial realization of the square ice model*. Brno: Brno University of Technology, Faculty of Mechanical Engineering, 2019. 81 p. Supervised by Dr. Nicolas Rougemaille

DECLARATION

I declare that I have elaborated my master's thesis on the theme of "Magnetic phases in an artificial realization of the square ice model" independently, under the supervision of the master's thesis supervisor and with the use of technical literature and other sources of information which are all quoted in the thesis and detailed in the list of literature at the end of the thesis.

As the author of the master's thesis I furthermore declare that, concerning the creation of this master's thesis, master's thesis, I have not infringed any copyright. In particular, I have not unlawfully encroached on anyone's personal copyright and I am fully aware of the consequences in the case of breaking Regulation § 11 and the following of the Copyright Act No 121/2000 Vol., including the possible consequences of criminal law resulted from Regulation § 152 of Criminal Act No 140/1961 Vol.

Brno ....

(author's signature)

Acknowledgement

First and foremost, I would like to express my utmost gratitude to Dr. Nicolas Rougemaille for introducing me to the exotic world of artificial spin systems and for his guidance and inspiring ideas. My gratitude also belongs to: Simon Le-Denmat for introducing me to the practice of MFM and his extensive technical support, Yann Perrin for sample fabrication and sharing his software solutions.

I also feel this is the right place to express my gratitude towards other people who supported my in my efforts: parents, family, work colleagues, friends and my girlfriend and soulmate Julie, who has been great support to me in many ways.

Bc. Ondřej Brunn

CONTENTS

1 Introduction **13**

2 Ice, spin ice and related models **15**
2.1 Background . . . 15
2.1.1 Frustrated systems . . . 16
2.1.2 Water Ice . . . 19
2.1.3 Spin ice materials . . . 20
2.2 Square lattice based models . . . 21
2.2.1 16 vertex model . . . 22
2.2.2 6 vertex model . . . 24
2.3 Artificial realizations of spin models . . . 27
2.3.1 Square lattice . . . 27
2.3.2 Z-shifted square lattice . . . 29
2.4 Thesis objectives and strategy . . . 30

3 Methods **35**
3.1 Micromagnetic simulations . . . 35
3.2 Sample fabrication . . . 37
3.2.1 Electron beam lithography . . . 37
3.2.2 Electron beam physical vapour deposition . . . 39
3.2.3 Lift-off . . . 39
3.3 Sample demagnetization . . . 40
3.4 Magnetic imaging . . . 42
3.4.1 Magnetic force microscopy . . . 42
3.4.2 Measurement details . . . 43
3.5 Analysis of measured data . . . 45
3.5.1 Pre-treatment . . . 46
3.5.2 Configuration extraction . . . 46
3.5.3 Vertex and spin mapping . . . 49
3.5.4 Magnetic structure factor . . . 49

4 Distorted square lattice **51**
4.1 Sample overview . . . 51
4.2 Results of fabrication . . . 52
4.3 Results of micromagnetic simulations . . . 53
4.4 Probing the phase diagram of DSL system . . . 55
4.4.1 Demagnetization efficiency assessment . . . 56

4.4.2 Captured configurations and vertex populations 57
4.4.3 AFM phase 60
4.4.4 SL phase 62
4.4.5 FM/line phase 63
4.4.6 Influence of exposure dose 65
4.4.7 Influence of gap size 67

5 Conclusion **69**

Bibliography **71**

List of appendices **77**

A Micromagnetic simulations **79**
A.1 Example of **MuMax³** input code 79

B Fabrication **81**
B.1 Fabrication process details 81

1 INTRODUCTION

For many years research in area of condensed matter physics was driven by efforts to understand low temperature states of natural materials. In some cases these low temperature states are unconventional and often counter-intuitive. Prime example may be crystalline compounds such as ice and spin ice materials, which remains disordered even at low temperature. The cause of this puzzling and surprising behaviour is phenomenon of frustration, that can be described as inability to satisfy all the interactions at the same time, thus the interactions are competing between each other.

The role of frustration in structurally ordered magnetic materials of natural origin was topic of extensive studies over past two decades. Experimental techniques used to probe those materials fails to provide local information about configuration of those systems and the systems must be studied in their full complexity. Over a decade ago artificial frustrated magnetic systems were introduced as a tool to study the phenomenon of frustration directly in real space with access to local information via magnetic imaging techniques. Those systems consists of arrays of nano-magnets that are typically fabricated by e-beam lithography techniques, which offers possibility to tune the system at will. In recent years not only nature inspired geometries are explored but also synthetic systems that targets effects or phenomenons that are not present in the nature are fabricated.

In this work we are working within the frame of those artificial frustrated magnetic systems. The main focus of this study is a new, previously not proposed geometry, that enable us to observe several magnetic phases by tuning one parameter of the system. The geometry is based on modification of seminal square lattice that may bee seen as distortion, thus we name the geometry distorted square lattice.

2 ICE, SPIN ICE AND RELATED MODELS

Main purpose of this chapter is to provide brief introduction and theoretical background relevant to the aim of the thesis. Section 2.1 covers the historical development, phenomenon of frustration and provides example of studied natural systems (water ice and spin ice materials). In section 2.2 the two-dimensional square lattice based models are introduced and their properties are discussed. Concept of artificial realizations of these spin models is presented in section 2.3 and examples of experimental realizations and their results are provided. Section 2.4 follows up with objectives and strategy of this thesis and the connection to previous experimental realizations is shortly discussed.

2.1 Background

In 1935 Linus Pauling [1] provided an explanation of Giauque's [2] zero-temperature entropy measurements of water ice. The explanation is based on a model in which each oxygen atom is surrounded by four hydrogen atoms, while two of them are placed at near position and two at far position (so called ice rules [3]). This Pauling's model of hydrogen structure in water ice is a prime example of a frustrated system [4].

The studies of water ice were followed up by various theoretical works focused on systems with similar properties. Magnetic model that mimics the ice rules of crystalized water was introduced by Anderson [5] when dealing with ordering in spinels with tetrahedral geometry. This model may be described as antiferromagnetically coupled Ising spins on tetrahedral lattice. Similar model was proposed for triangular lattice by Wannier [6]. Those two papers represents cornerstone of frustrated magnetism research.

In the 1960's and 1970's models inspired by Pauling ice model were studied extensively and solved exactly in two dimensions [7–9]. This is the case for Slater-KDP model [10] of ferroelectric, Rys F model [11] of antiferroelectric and ice model itself. These models are often referred to as ice-type models as they all incorporates the ice rules. Nowadays generalised ice-type models are known as vertex models [12, 13].

In the 1990's study of frustrated magnets and related models received experimental boost in form of so called *spin ice materials*, which were introduced by Harris [14]. Typical spin ice materials are rare-earth pyrochlore oxides such as $Ho_2Ti_2O_7$ or $Dy_2Ti_2O_7$ [4]. Those materials enabled scientists to reach experimentally the vertex models previously theoretically studied. However there is several disadvantages while experimentally studying those systems. Firstly, the experimental techniques do not provide local information about magnetic configuration as the acquired information

is averaged over the bulk of the sample. Also the measurements must be done at low temperatures and the systems must be studied in their whole complexity.

Experimental possibilities of studying frustrated magnetism and vertex models were significantly broadened in 2006 by Wang [15] in form of artificial frustrated magnetic systems. These systems are often referred to as *artificial spin ice* as they were introduced with intention to mimic properties of natural spin ice materials [16]. Thanks to the tunability through nanofabrication, possibility of accessing both local and global information, possibility to measure at room temperature and "easy of use" these systems became great interest of the community in recent years [16–18].

2.1.1 Frustrated systems

Frustration is the inability to simultaneously satisfy all the bonds/interactions within the system. In condensed matter systems two main sources of frustration are recognised. Frustration may arise either from strong structural disorder within the compound or geometry of the lattice combined with the type of the interactions (e.g. antiferromagnetic) [16]. The case of structural disorder leads to spin glass phenomena [16, 19] and will not be further discussed in this thesis. The other case, frustration that comes from the lattice geometry, will be the main focus of this subsection (resp. thesis) and will be referred to as *geometrical frustration*.

In the absence of disorder, frustration in magnetic systems (both artificial and natural) may arise from the lattice geometry and the nature of the interactions [18]. This may be illustrated using simple polygons such as triangle and hexagon with Ising like variables (+1/-1) placed in their corners [18, 20, 21]. In the context of frustrated magnets this variable may represent spin orientation (e.g. spin up/spin down). Now consider nearest-neighbour interaction that prefers alternating arrangement (i.e. antiferromagnetic). Figure 2.1a illustrates that antiferromagnetic interaction on triangular lattice leads to frustration of at least one bond (side of triangle) in any ground state configuration. Contrary to that, in case of hexagon, we are able to find the configuration where all the bonds are satisfied (Fig. 2.1b). This may by generalized into a rule (for ground state configuration), that in case of antiferromagnetic interaction the polygons with odd number of corners are always frustrated and the polygons with even number of corners are not. It is straightforward that in case of ferromagnetic interaction (and perfect ground state ordering) all polygons are unfrustrated.

In case of hexagon there are just two possible ground state configurations (unfrustrated), whereas for triangle there is six of them (all frustrated). When incorporated as building blocks into larger system (lattice) these two geometries behave differently. In case of hexagonal lattice the number of possible ground state configu-

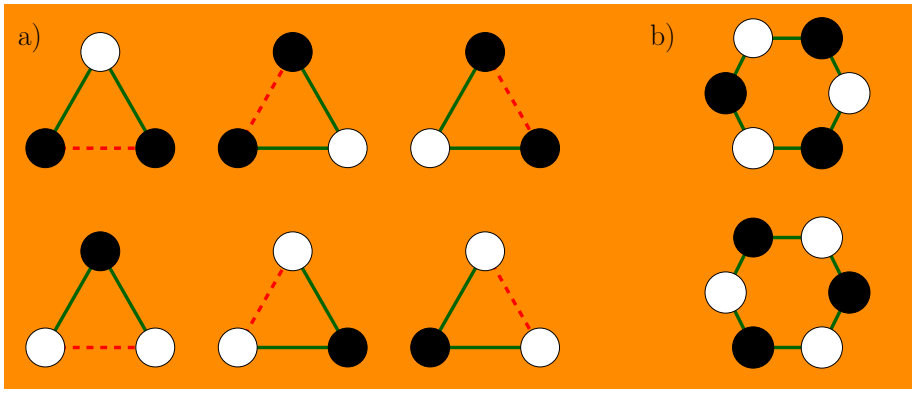

Fig. 2.1: Possible ground state configurations for (a) triangle and (b) hexagon with antiferromagnetic interaction. Black and white circles correspond to spins pointing in-plane and out-of-plane respectively. Solid green line represents satisfied bond and red dashed line represents frustrated bond. The colours (black, white and orange) are chosen on purpose, to mimic typical contrast used for magnetic force microscopy images (see Fig. 2.4).

rations does not depend on the system size. In other words, if we pick configuration of first hexagon, there is only one possibility how to link another hexagon to its side (Fig. 2.2). For corner sharing triangular lattice the number of possible ground state configurations is size dependent and it increase faster than the system size (Fig. 2.3). Thus the ground state of such a system is macroscopically degenerate (number of possible ground state configurations increases exponentially with the number of triangles) [18], which leads to extensive magnetic disorder of the system. Because of that, even at low temperature statistical entropy per site remains finite (also called residual entropy), and the system is never frozen – the spins fluctuate down to very low temperature [18].

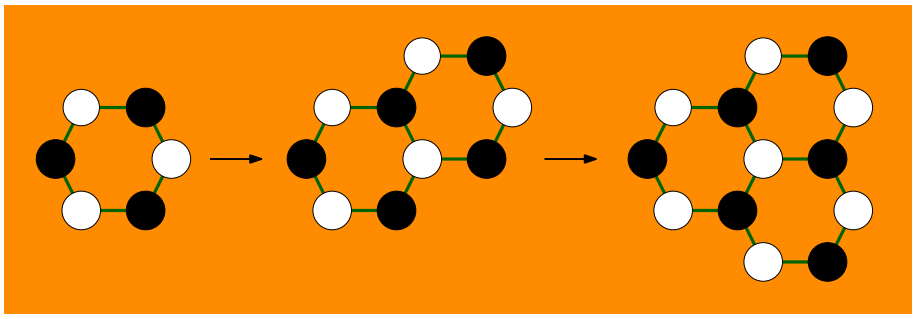

Fig. 2.2: Building of hexagonal lattice with antiferromagnetic interaction and ground state ordering. The configuration of the whole system is given by first hexagon and it does not depend on the system size.

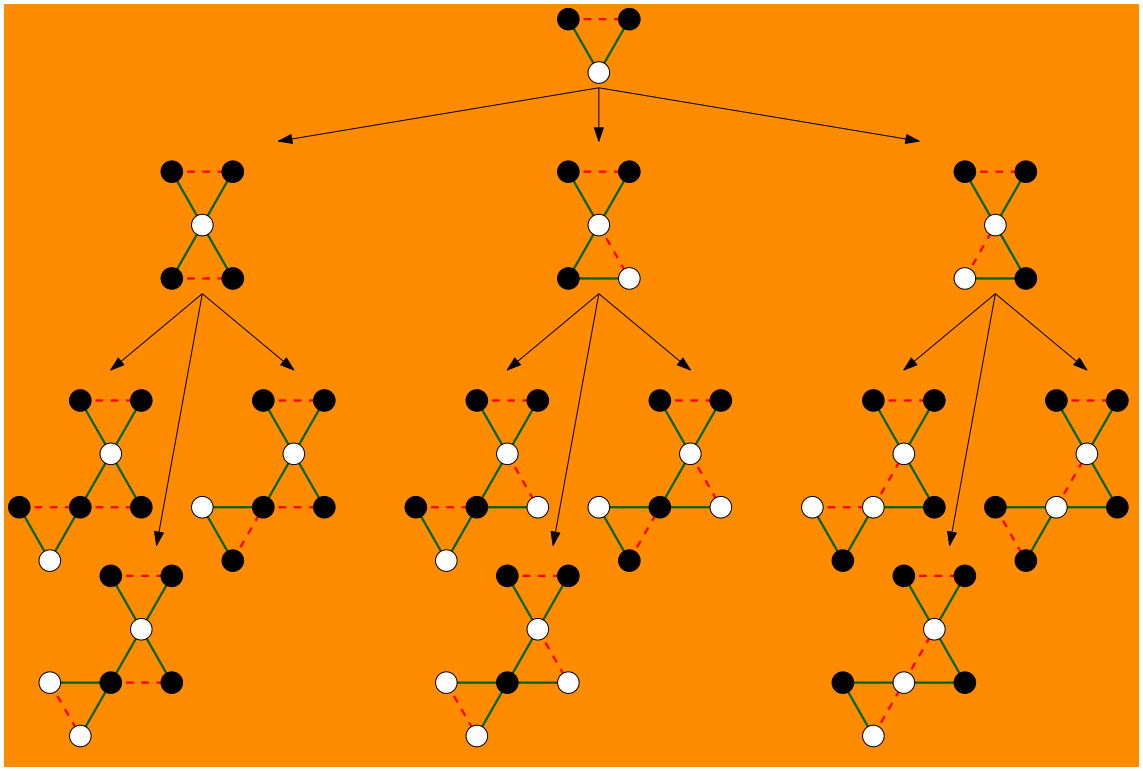

Fig. 2.3: Building of corner sharing triangular lattice with antiferromagnetic interaction and ground state ordering. The degeneracy of the ground state configuration increases with the system size. When adding next triangle to the lattice there are always three energetically equal possibilities.

The example of experimental realization of those two geometries is provided in Figure 2.4. It is visible that for hexagonal lattice (Fig. 2.4a) we see almost perfect magnetic ordering, whereas for triangular lattice (Fig. 2.4b) we see disordered system.

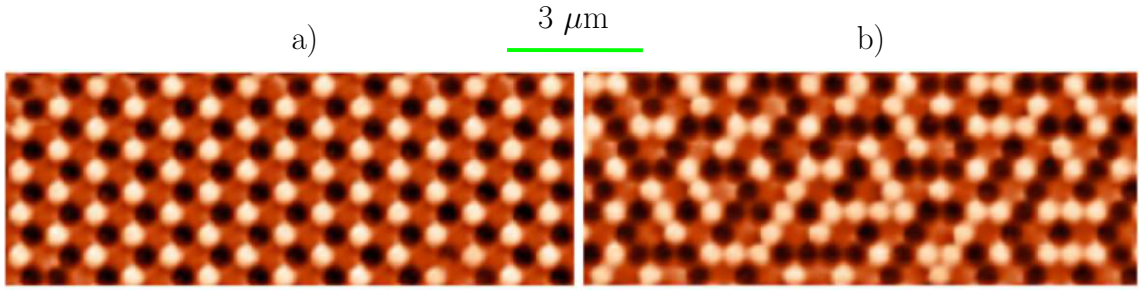

Fig. 2.4: Arrays of antiferromagnetically coupled nanodisks with (a) hexagonal and (b) triangular geometry imaged by magnetic force microscopy at room temperature. Black and white contrast corresponds to magnetization of the disks (spin in-plane/out-of-plane), orange is neutral background. Adapted from [18].

2.1.2 Water Ice

In previous subsection example of 2D geometrically frustrated system was provided and resulting properties were discussed. The same phenomenon may be observed in 3D system. The canonical example (and historically first studied frustrated system) is solid phase of water - ordinary ice (hexagonal phase I_h to be precise).

In this phase the oxygen atoms are located at the centre of corner sharing tetrahedra, also known as pyrochlore lattice. Each oxygen atom then have four neighbouring oxygen atoms, each connected through intermediate hydrogen atom (Fig. 2.5a). The hydrogen atoms are not placed in the middle of link between two oxygen atoms, but rather closer to one of them [1]. Thus in total there is 16 possibilities how to arrange hydrogen atoms around oxygen atom (4 hydrogen atoms, 2 possible positions for each). The lowest energy state has 2 atoms in close position (covalent bond) and 2 in far position (hydrogen bond), this is often shown by displacement vectors pointing in (close position) and out (far position) – Fig.2.5a). There is 6 possible configurations that fulfil this condition two in/two out (also known as ice rules [3], thus the ground state is six times degenerate. The ice rules itself comes from the strong chemical binding energy of water molecule and therefore electrostatic interaction energy is not minimized. This leads to frustration of effective proton-proton interaction.

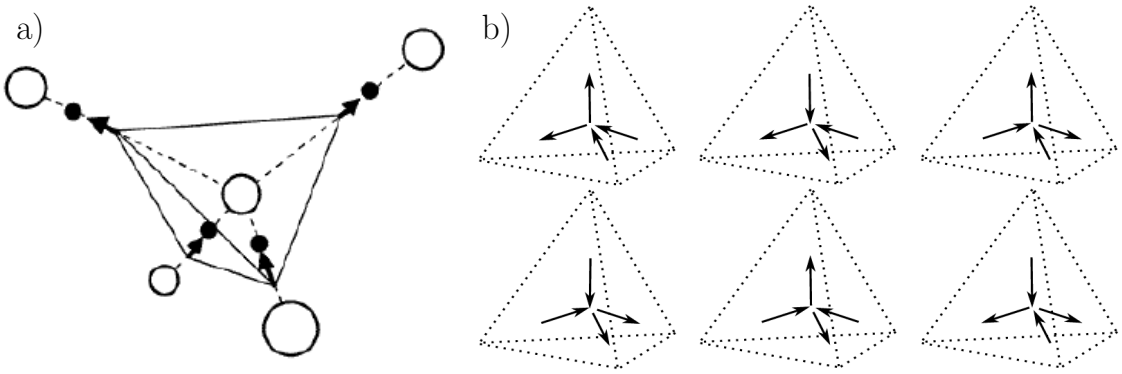

Fig. 2.5: a) Water molecule arrangement in ice, oxygen (open circle) is placed in the centre of tetrahedra and is connected to 4 protons (filled circles). The arrows pointing in/out represents close/far position respectively. b) Six possible ground state configurations (two in/two out condition), given by different orientation of central molecule of water. a) adapted from [4] and b) from [20].

When connected into corner-sharing tetrahedron lattice the system behaves similar to a triangular lattice presented in previous subsection. The ground state of such a system is again macroscopically degenerate (number of possible ground state configurations also grows faster than the system itself), which leads to disordered

proton structure in water ice. The residual entropy of ice was famously calculated by Pauling [1] and later confirmed by calorimetric experiment conducted by Giaque [22].

2.1.3 Spin ice materials

As suggested by the name, the spin ice materials are natural compounds that exhibit properties similar to a water ice (most notably the residual entropy) [4]. Typical spin ice materials are rare earth pyrochlores such as $Ho_2Ti_2O_7$ or $Dy_2Ti_2O_7$ [4, 23], and their study was initiated in 1997 by Harris [14]. The magnetic ions of these compounds (Ho^{3+} or Dy^{3+}) are located at junctions of corner-sharing tetrahedron lattice (also called pyrochlore lattice) – see Fig. 2.6a. These ions carry magnetic moments that are, thanks to strong single ion anisotropy, aligned along the line connecting centres of two corner-sharing tetrahedra (Fig. 2.6b) and may be described as classical Ising like spins at low temperatures [23]. Magnetic moments thus may be seen as an analogy of the proton positions in water ice (Fig. 2.6c), as they point in/out from the centre of tetrahedron.

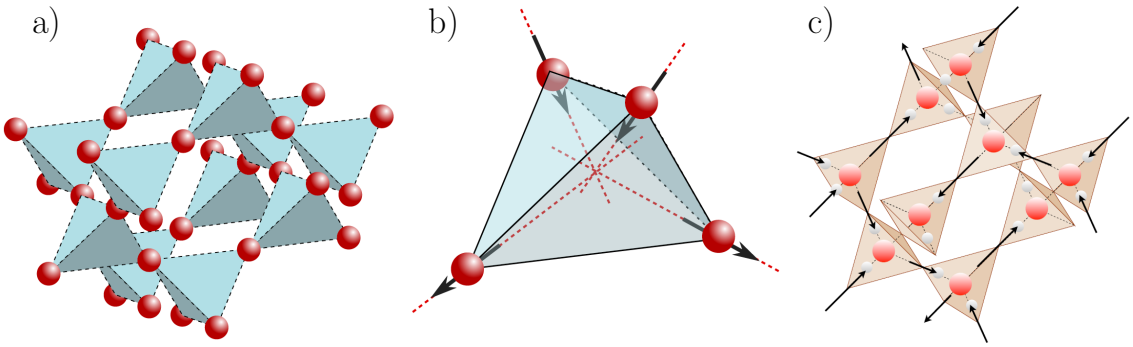

Fig. 2.6: a) Pyrochlore lattice with magnetic ions (red spheres) placed at junctions of corner-sharing tetrahedra. b) Magnetic moments of these ions act as Ising spins and can point either inward or outward from the centre of tetrahedra. c) Analogy between structure of water ice (I_h phase) and pyrochlore oxides, the red and white spheres represents oxygen and hydrogen atoms, respectively. The arrows represent spins (for pyrochlores) and hydrogen positions (for water). a) and b) adapted from [20], c) adapted from [23].

Because of the topological similarity pyrochlores may be seen as magnetic equivalent of water ice. These materials are in fact frustrated, the ice rules (two in/two out) for ground state configuration are valid and they exhibit residual entropy – measured by Ramirez [24] for $Dy_2Ti_2O_7$ in 1999.

2.2 Square lattice based models

In previous two subsections the structure of water ice and pyrochlore crystals were discussed. Naturally, both of these compounds are three-dimensional. One may imagine that it is helpful to reduce the dimensionality of the problem to ease the solution. In fact, only 2D models similar to water ice were solved exactly [7–9], whereas the 3D ice-type models are solved only for special states [13]. The 2D analogue of water ice is possible to obtain by projecting the pyrochlore lattice onto a plane (Fig. 2.7a). Each tetrahedron is projected into a square, creating chequerboard pattern (Fig. 2.7b). More importantly the spins are also projected and they are located at corners of projected squares (again pointing inward or outward of the square). Thus we obtain a square lattice with coordination number 4 (at each junction 4 spins are meeting), that mimics the properties of water ice (resp. pyrochlore crystals) as each spin have 2 possible orientation. The configuration of such a lattice is possible to describe by vertex model, which describes local configuration of spins for each grid point (Fig. 2.7c).

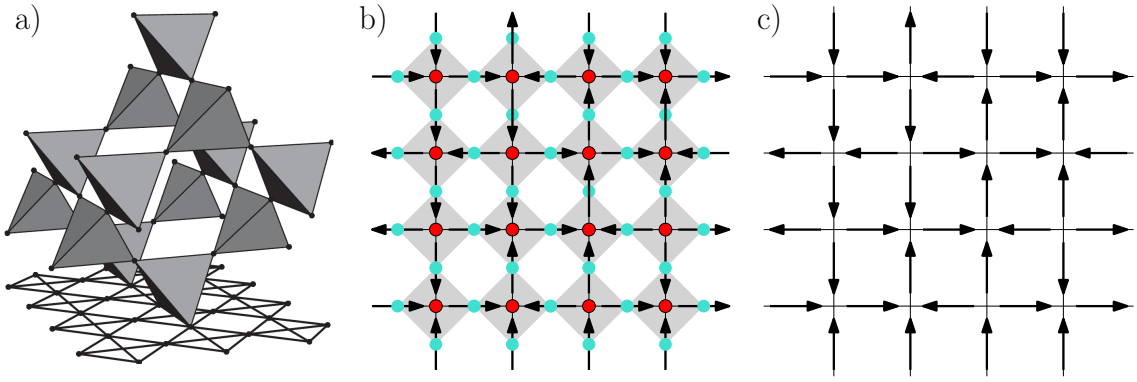

Fig. 2.7: a) Projection of pyrochlore lattice onto a plane, projection is done alongside (100 direction). b) Projected 2D square lattice (also known as 2D pyrochlore lattice). Analogies with pyrochlore lattice (blue circles represent rare-earth ions, arrows represent magnetic moments) and water ice (red dots represent oxygen atoms, arrows represent hydrogen position) are illustrated. c) Vertex representation of b). a) adapted from [25].

Even though the 2D square lattice have different dimensionality, it provides good approximation of its 3D counterpart and is exactly solvable [13].

2.2.1 16 vertex model

The most general vertex model based on a square lattice geometry (introduced in Fig. 2.7) is the 16 vertex model, which includes all possible configurations. Each vertex is characterized by 4 Ising like variables (represented by spins with 2 possible directions), thus we have $2^4 = 16$ possible vertices (see Fig. 2.8), as the name of the model suggests.

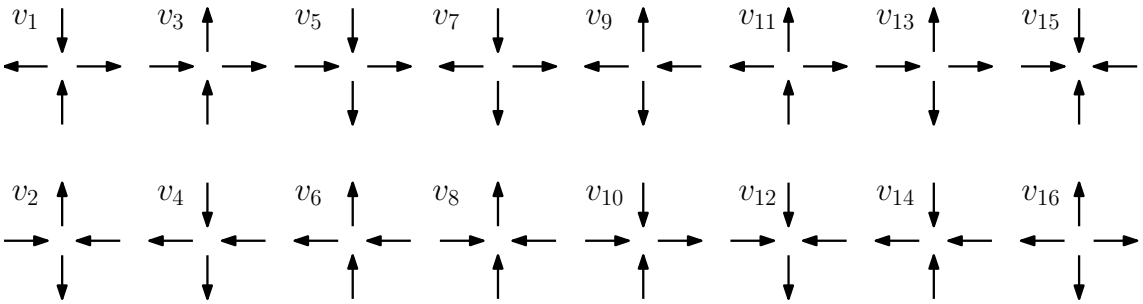

Fig. 2.8: All possible vertex configurations for square lattice geometry.

An energy ϵ_i may be assigned to each vertex v_i. Thus total energy of a local magnetic microstate (such as 4 by 4 vertices in 2.7c) is a sum of energy of individual vertices:

$$E_{\text{tot}} = \sum_{i=1}^{16} \epsilon_i n_i, \tag{2.1}$$

where n_i is number of v_i vertices within the system.

When one consider spin-reversal symmetry (e. g. $v_1 \rightarrow v_2$) and rotational invariance by $\frac{\pi}{4}$ (e. g. $v_3 \rightarrow v_5$), it is possible to divide vertices into 4 categories - vertex types (Fig. 2.9). In fact, this division is very meaningful as vertices of same vertex type are equal in energy. This may be shown by assigning coupling strength between nearest- (J_1) and second-nearest (J_2) neighbours within an individual vertex (see Fig. 2.10a,b). The energy of individual vertex is than given as a sum of all 6 neighbouring interactions (with - sign for favourable and + sign for unfavourable alignment[1], illustrated in Fig. 2.10c). Thus the energy levels of vertex types are:

$$\begin{aligned} E_{\text{I}} &= -4J_1 + 2J_2, \\ E_{\text{II}} &= -2J_1 + 2J_1 - 2J_2 = -2J_2, \\ E_{\text{III}} &= -2J_1 + 2J_1 - J_2 + J_2 = 0, \\ E_{\text{IV}} &= 4J_1 + 2J_2. \end{aligned} \tag{2.2}$$

It is reasonable to assume that coupling strength of nearest neighbours is stronger than of second-nearest ($J_1 > J_2$), thus the energy increase from Type I to Type IV.

[1] Antiferromagnetic interaction between the spins is considered.

A charge q can be assigned to each vertex configuration v_i as:

$$q_i = \sum_{v_i, j=1}^{4} \sigma_j, \tag{2.3}$$

where $\sigma = +1$ for spin pointing inwards and $\sigma = -1$ for spin pointing outwards of the vertex v_i. Therefore type I and type II vertices have no charge ($q = 0$), type III vertices have charge $q = \pm 2$ and type IV vertices have charge $q = \pm 4$ (see Fig. 2.9).

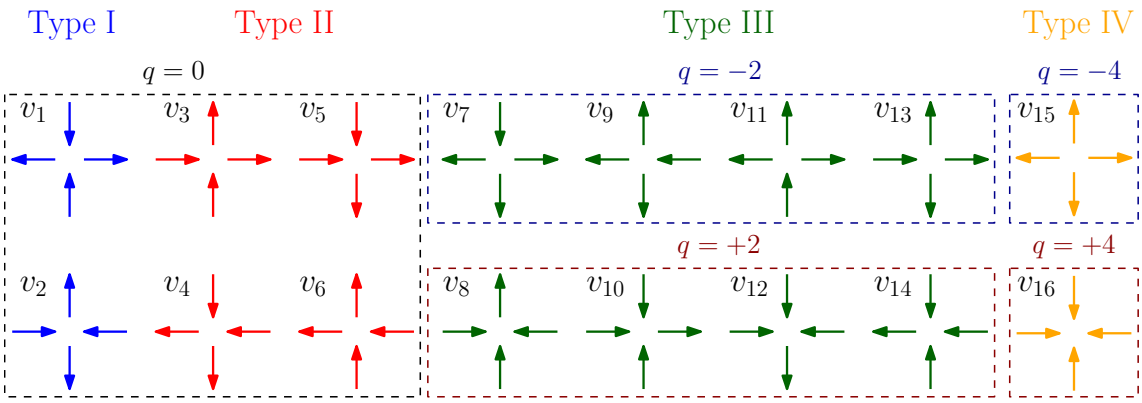

Fig. 2.9: 16 possible vertex configurations divided into 4 categories – vertex types. Each vertex configuration v_i have assigned charge q.

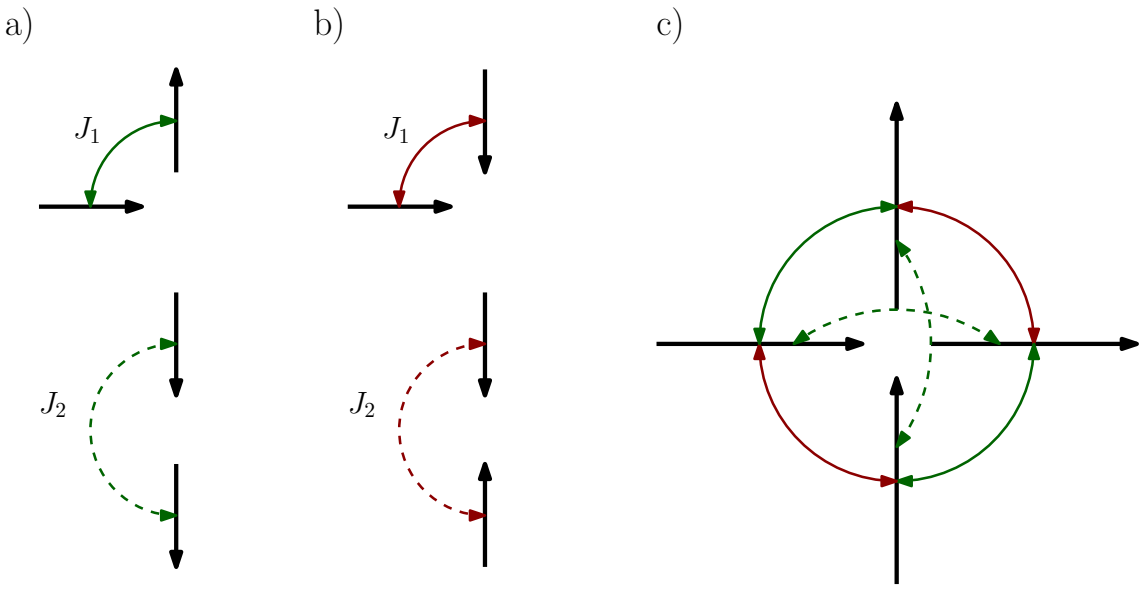

Fig. 2.10: Favourable (a) and unfavourable (b) alignment of nearest (J_1, solid line) and second-nearest neighbours (J_2, dashed line). c) All interactions within type II (v_3) vertex.

2.2.2 6 vertex model

In the 6 vertex model (also known as ice-type model), only vertices that satisfy the ice rules [1, 3] (two in/two out pointing spins) are considered. This condition is fulfilled by the type I (2 configurations, $v_{1,2}$) and type II vertices (4 configurations, v_{3-6}). Therefore 6 different vertex configurations are allowed (see Fig. 2.11), as the name of the model suggests. Generally, each of the allowed configurations will have

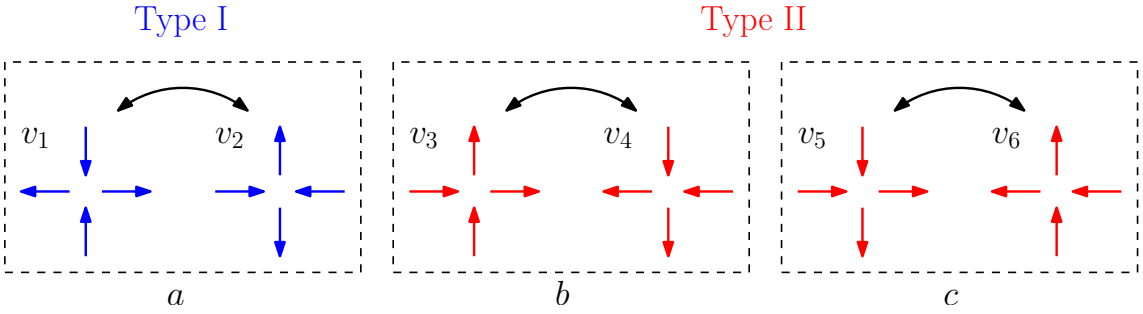

Fig. 2.11: 6 vertex model possible configurations that satisfy the ice rule (two in/two out). According to the spin reversal symmetry (eg. $v_1 \rightarrow v_2$), the system may be described by 3 parameters (statistical weights) a, b, c.

distinct energy ϵ_i. By tuning these energy values, three characteristic models may be reached (Slater-KDP model, Rys-F model and ice model) [13].

Rys-F model

Rys (1963) [11] proposed that model of anti-ferroelectric may by obtained by appropriate choice of energies:

$$\epsilon_1 = \epsilon_2 = 0, \;\; \epsilon_3 = \epsilon_4 = \epsilon_5 = \epsilon_6 > 0. \tag{2.4}$$

The ground state configuration of such a model consists of type I vertices (v_1 and v_2), that alternates in horizontal and vertical direction. Therefore the configuration is anti-ferroelectric (resp. anti-ferromagnetic for magnetic system) – see Fig. 2.12a.

Slater-KDP model

Slater (1941) [10] suggested that ferroelectric low-energy configuration of KH_2PO_4 (potassium dihydrogen phosphate – KDP) could be obtained by choosing proper energies:

$$\epsilon_3 = \epsilon_4 = 0, \;\; \epsilon_1 = \epsilon_2 = \epsilon_5 = \epsilon_6 > 0. \tag{2.5}$$

The ground state configuration is than dominated either by v_3 or v_4 vertices (spin-reversal symmetry). Thus creating ferroelectric ordering (resp. ferromagnetic

for magnetic system). Alternatively $\epsilon_5 = \epsilon_6 = 0$ instead of $\epsilon_3 = \epsilon_4 = 0$ leads to the same behaviour. Both possible ground state configurations are illustrated in Fig. 2.12b,c.

Ice model

When discussing the properties of water ice, we noted that there is six possible ground state configurations around each oxygen atom (i.e. vertex points) – see Fig. (2.5). Therefore in ice model energies of all 6 vertices are set to be equal (and zero):

$$\epsilon_1 = \epsilon_2 = \epsilon_3 = \epsilon_4 = \epsilon_5 = \epsilon_6 = 0. \tag{2.6}$$

The ground state configuration of such a model is disordered and exhibits residual entropy. Both type I and type II vertices are present and their ratio is given by number of possible configurations for each type (2:4 for type I:type II, respectively).

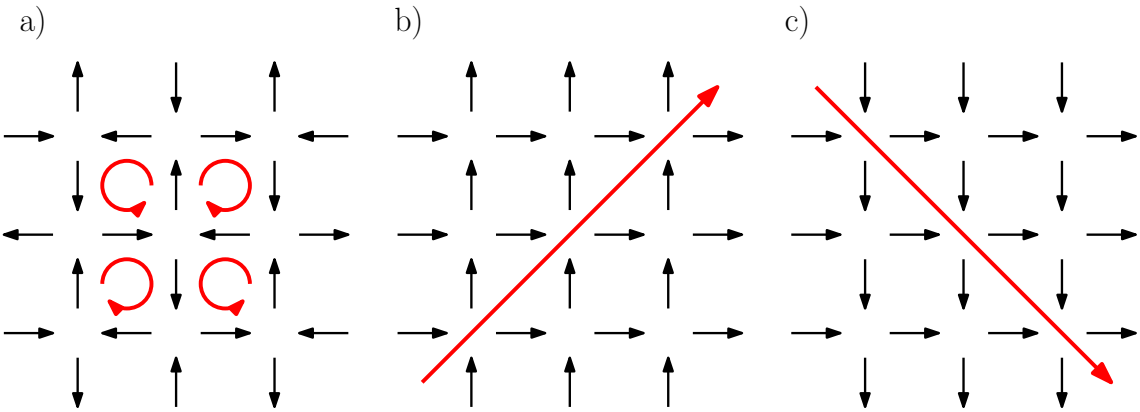

Fig. 2.12: a) Ground state configuration of Rys-F model with anti-ferroelectric (resp. anti-ferromagnetic) ordering, only type I vertices (v_1 and v_2) are present. Polarization (resp. magnetization) loops (represented by red colour) alternates in direction, thus neglects each other. If all the spins are reversed, vertices v_1 and v_2 switch places. b), c) Ground state configurations of Slater-KDP model with ferroelectric (resp. ferromagnetic) ordering, only type II vertices are present (v_3 in b) and v_5 in c)). Total polarization (resp. magnetization) of the system is illustrated by the red arrow. By reversing all the spins we change the vertex configuration from v_3 to v_4 (for b)) and from v_5 to v_6 (for c)), the total polarization (resp. magnetization) reverses accordingly.

Phase diagram of the 6 vertex model

In previous subsection the 6 vertex model was described from energy point of view (energy ϵ_i was assigned to given vertex v_i) [23]. Therefore it is possible to assign statistical weight to each vertex as $\omega_i \propto \exp(-\epsilon_i)$ where ϵ_i is energy of vertex v_i. Assuming spin-reversal symmetry only three weights (a, b, c) allow the description of the system [13] (see Fig. 2.11). Four different regions may be found in the phase diagram of a magnetic system on a square lattice (see Fig. 2.13 [23]:

- **Anti-ferromagnetic (AF) phase** (F model): the energy of a-vertices is set to zero, energy of b- and c-vertices is set to be equal and positive, i.e. $a > b = c$ (more generally $a > b + c$).
- **Ferromagnetic (FM) phase** (KDP model): the energy of b- or c- vertices is set to zero, energy of all others is set to be equal and positive, i.e. $b > a = c$ or $c > a = b$ (more generally $b > a + c$ or $c > a + b$).
- **Spin-liquid (SL) disordered phase** (Ice model): the energy of all vertices is set to be equal (often zero), i.e. $a = b = c$ (more generally $a, b, c < \frac{1}{2}(a+b+c)$).

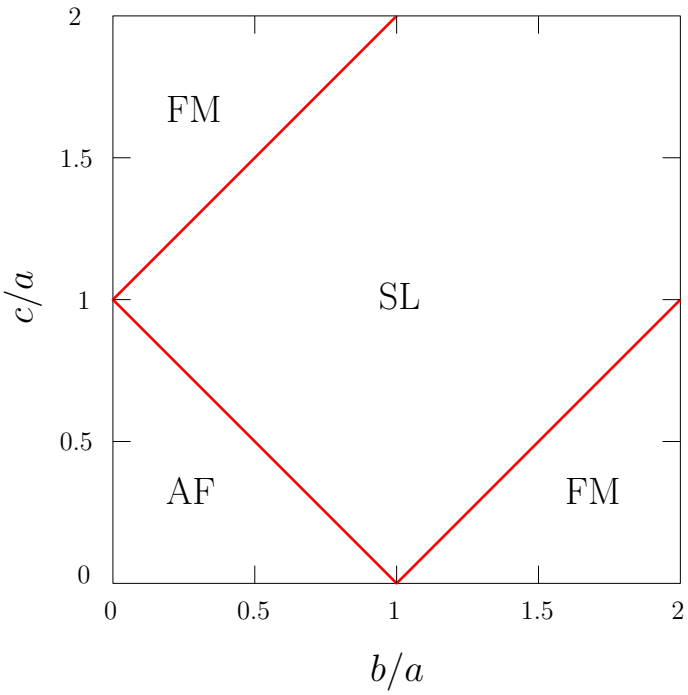

Fig. 2.13: The phase diagram of the 6 vertex model. AF, FM, SL stands for anti-ferromagnetic, ferromagnetic and spin-liquid phase, respectively. a, b, c are statistical weights associated with vertices according to 2.11. Adapted from [23].

2.3 Artificial realizations of spin models

The development of micro- and nanofabrication methods opened new possibilities for studying geometrical frustration and related phenomena in form of artificial frustrated magnetic systems. Main motivation for these systems were to mimic physics of water ice and spin ice materials, thus these systems are often referred to as *artificial spin ice* [16, 17]. These 2D systems consist of interacting elongated nano-magnets, that are arranged into a lattice of targeted geometry. Because of the size and shape these magnets are single-domain, thus can be described by classical Ising spin. Therefore these systems may be interpreted as spin models and can be described by models of statistical mechanics (e.g. vertex models, introduced for square lattice in section 2.2).

Compared to natural spin ice materials (subsection 2.1.3), artificial systems provide several advantages. In subsection 2.1.1 we described how the frustration may arise from the system geometry. In case of artificial systems, the geometry may be designed and tuned at will through the fabrication processes. The experimental methods used to characterize artificial systems are often more convenient than methods used to probe their natural counterparts. For example, artificial spin system can be studied by Magnetic Force Microscopy (MFM) at room temperature without applied external field. Contrary to that, for studying natural spin ice materials low temperatures (typically < 20 K) and external fields are often required (e.g. neutron diffraction on pyrochlore crystals). Moreover artificial systems can be characterized directly in real space, thus both local and global information about magnetic ordering is available (in case of natural spin ice materials information is averaged over the bulk of the sample).

As stated previously, artificial systems were firstly introduced to mimic the physics of spin ice materials (pyrochlore crystals). Therefore, studied geometries were deduced from the 3D pyrochlore latice – 2D square lattice [15] (projection of pyrochlore lattice onto a plane, illustrated in Fig. 2.7) and 2D kagome lattice [26] ([111] planes of pyrochlore lattice). These initial studies inspired many research groups and various geometries were studied (reviews [16–18]). Here geometries (and their experimental realizations) based on 2D square lattice will be discussed, as this geometry is the main focus of this thesis.

2.3.1 Square lattice

This geometry is based on projection of 3D pyrochlore lattice onto a plane (see Fig. 2.7 for details). Figure 2.14 illustrates concept of artificial realization of square lattice spin system. Elongated oval-shaped single-domain magnets are centred on

bonds of a square net. Therefore their magnetic moments act as an Ising-like spins and effectively creates 2D square spin system, that can be described by vertex models (2.2). This geometry was introduced and experimentally realized (see Fig. 2.15a,b) by Wang et al. [15] with hope to mimic the exotic low-energy physics of spin ice materials.

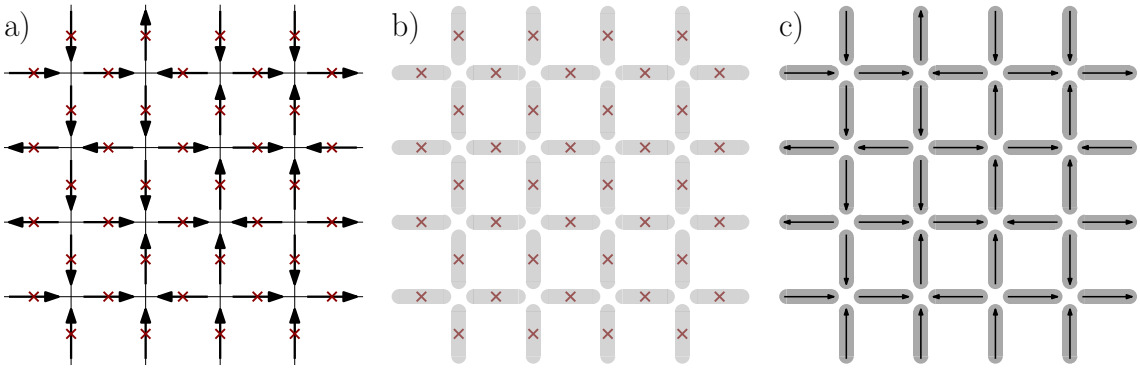

Fig. 2.14: a) Spin system obtained by projection of 3D pyrochlore lattice onto a plane (from Fig.2.7), red marks indicates centres of vertex-vertex links. b) Elongated oval--shaped single-domain magnets are centred between vertex points. c) Artificial spin system modelled by square lattice geometry.

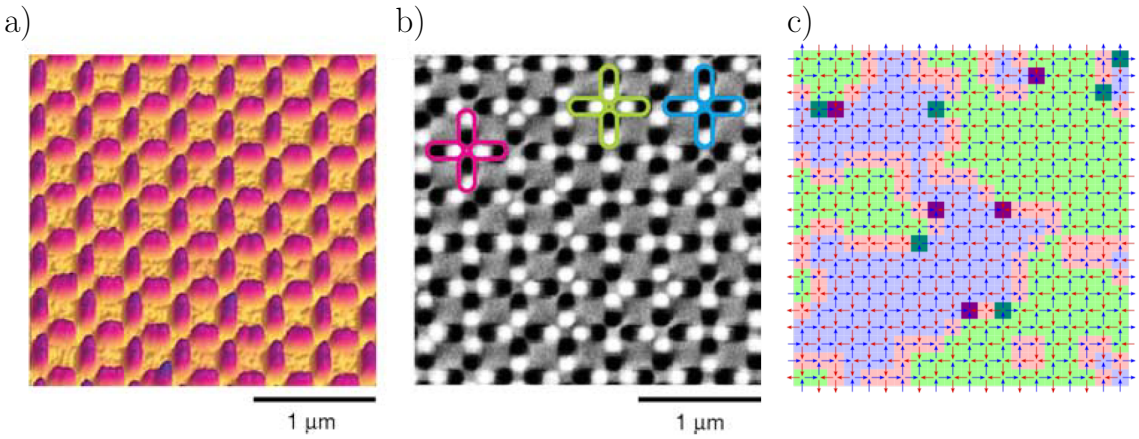

Fig. 2.15: a) Atomic force microscopy image of artificial square system. b) Related magnetic force microscopy image, type I (pink), II (blue) and III (green) vertices are highlighted. Both images adapted from [15]. c) Typical ground-state like configuration of artificial square lattice, patches of type I vertices (blue and green) are separated by type II vertices (red) and type III vertices (dark green and magenta).

Even though the frustration is present within the system – only 4 from 6 interactions within each vertex are satisfied in best case scenario (type I vertices), it does not lead to macroscopically degenerate disordered ground-state configuration. This

behaviour is consequence of the fact that magnetostatic interactions are stronger for nearest neighbours (perpendicular, coupling strength J_1) than for second-nearest neighbours (collinear, coupling strength J_2), described in Fig. 2.10. Therefore energy of type I vertices is smaller than for type II vertices, and the system orders towards an anti-ferromagnetic ground state [15, 18] (similar to Rys-F model). Typical experimental ground-state like configuration (Fig. 2.15c) is dominated by type I vertices with type II vertices acting as domain walls (small number of type III vertices is incorporated into this domain walls).

Although the system failed to provide experimental realization of spin-liquid phase, it was and is often used as benchmark to prove that protocol used to bring sample to its low-energy state was efficient (e.g. [20], also this thesis – in fact Fig.2.15c is configuration of such a calibration lattice).

2.3.2 Z-shifted square lattice

In the same year (2006) Möller and Mossner provide theoretical proposal [27] how to reach the spin-liquid phase predicted by the square ice model. The goal is to level-up the energy of type I and type II vertices ($E_{\mathrm{I}} = E_{\mathrm{II}}$), thus the vertex ground state would be six-time degenerate (as for water ice – Fig. 2.5b). From Eq. 2.2 we can deduce that to reach this condition the coupling strengths J_1 and J_2 must be equal. The proposal is based on tuning the ratio of coupling strengths J_1/J_2 by vertically shifting one of the sublattices of square lattice (see Fig. 2.16a) by distance h. Such a vertical shift reduces coupling strength J_1 (nearest neighbours, perpendicular magnets) while leaving coupling strength J_2 (second-nearest neighbours, collinear magnets) untouched.

Experimental realization of this proposal was provided by Perrin et al. [28] (more detailed in [20]) and was successful in capturing of disordered spin-liquid phase. By shifting the parameter h it is possible to probe different phases of the 6 vertex model (Fig. 2.13). When $h = 0$ nm, the geometry is equivalent to previously described square lattice, which can be again used as calibration lattice (experimental configuration in Fig. 2.16b).

At some critical height h_c the degeneracy is reached ($E_{\mathrm{I}} = E_{\mathrm{II}}$), and all 6 vertex configurations (allowed by ice rules) are equally likely to occur (ideally the vertex populations would be 1/3 type I and 2/3 type II). This leads to macroscopically degenerate low-energy manifold that is disordered and is in fact realization of spin--liquid phase (Ice model). Fig. 2.16c shows the vertex configuration for vertical shift $h = 80$ nm (close to disordered phase, vertex populations are: 52 % (type I), 39 % (type II) and 9 % (type III). The configuration itself may be described as small patches of type I diffused in background (bigger patches) of type II vertices. Most

significant characteristics of spin-liquid phase were observed for lattices with vertical shift $h = 100$ nm.

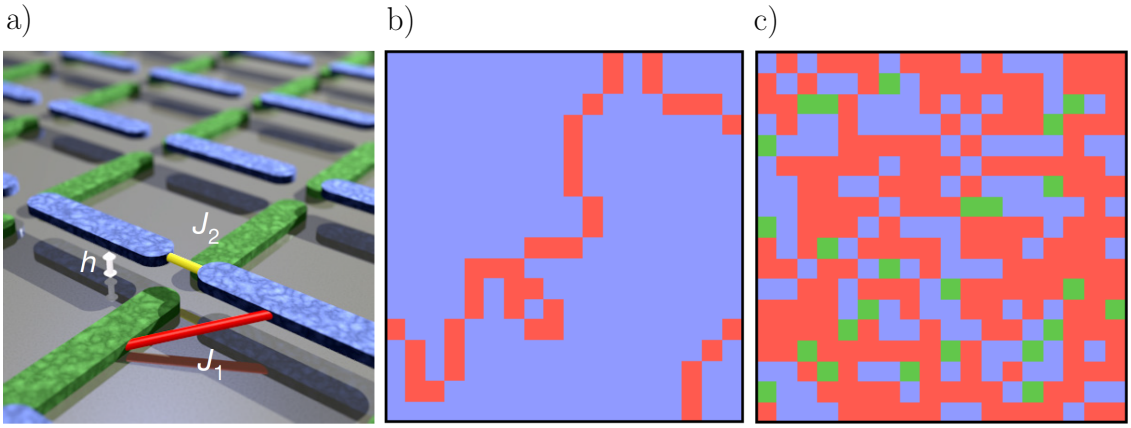

Fig. 2.16: a) Schematics of z-shifted square lattice geometry, sublattice (blue) is vertically shifted by h. Resulting experimental low-energy configurations for (b) $h = 0$ nm (square lattice) and (c) $h = 80$ nm (z-shifted square lattice). Blue, red and green squares represents vertices of type I, II and III respectively. All figures adapted from [28].

2.4 Thesis objectives and strategy

The main goal of this work is to provide experimental scan through different phases of square spin model (6 vertex model), that were introduced previously in subsection 2.2.2. Previous experimental works, based on square lattice geometry and its modifications, provided evidence of different low-energy manifold configurations (magnetic phases): square lattice [15] (AFM phase), z-shifted square lattice [20, 28] (AFM, SL phase), connected square lattice with holes [29] (AFM, SL, FM/line phase) or square lattice with circular islands [30] (AFM, SL, FM/line phase).

In this work we introduce previously theoretically not proposed modification of square lattice, that could enable reaching different low-energy configurations determined by tuning of single parameter of the system geometry (similar to h in z-shifted square lattice). This modification may be seen as distortion, thus we named it distorted square lattice (DSL). Such a system could provide several advantages over previously experimentally realized ones. Firstly, the system is effectively two-dimensional, which leads to easier fabrication and magnetic imaging (compared to z-shifted square lattice). The system can be fabricated both in thin (several nm) and thick (approx. 25 nm) variant of magnetic layer (unlike the square lattice with

circular islands, that require thin magnetic layer to work). The nature of the interaction is similar to a regular square lattice (unlike the connected square lattice with holes).

The modification itself is shown in Fig. 2.17 and can be described by single geometrical parameter – angle α (see Fig. 2.17a). If $\alpha = 45°$, the system is equivalent to regular square lattice. When increased above this value, the lattice starts to be modified (distorted), which leads to uneven distance between two pairs of collinear magnets for each vertex (base gap g_1 for one pair and bigger gap g_2 for second pair). As the modification is altered in both principal direction of the square lattice, it does not lead to rectangular lattice (also experimentally realized [31]), but to the distorted square lattice (Fig. 2.17c).

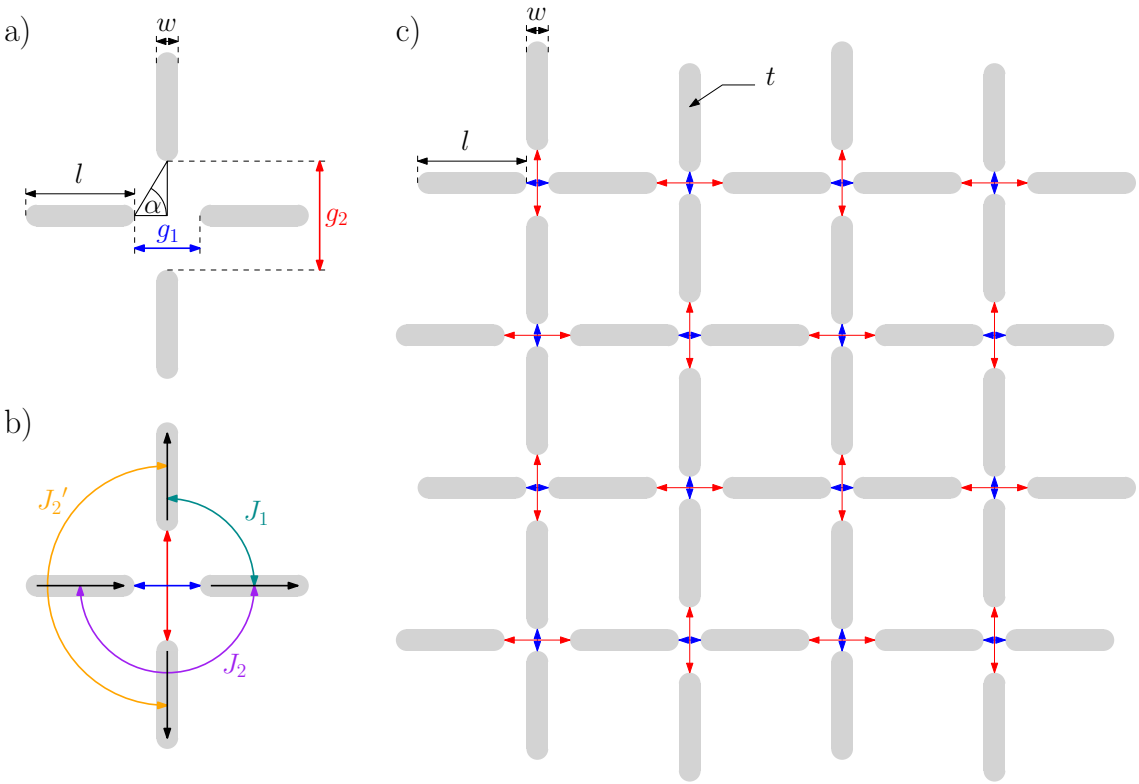

Fig. 2.17: a) Artificial realization of DSL vertex by 4 magnets, basic geometrical parameters are illustrated: width w, length l, distortion angle α, base gap g_1 and increased gap g_2. b) Coupling strengths in DSL vertex configuration: J_1 (perpendicular pair), J_2 (collinear pair with gap g_1) and J_2' (collinear pair with gap g_2). c) DSL system of 4 by 4 vertices.

Idea behind the modification is similar to a z-shifted square lattice. Again we aim to tune the ratio of coupling strengths between nearest (perpendicular, J_1) and second-nearest neighbours (collinear, J_2). The distortion leads to two pairs of collinear magnets, that have distinct magnet to magnet distance (gap). Therefore

we must distinguish coupling strength J_2 (collinear magnets with base gap g_1) and coupling strength J_2' (collinear magnets with increased gap g_2), illustrated by Fig. 2.17b. When α is further increased (above 45°) J_1 is reduced, J_2 is constant and J_2' is reduced. Thus the ratio $J_1/(J_2 + J_2')/2$ is tunable and it is possible to find α_c for which the ratio equals to 1 and the condition for spin-liquid phase is reached. The effect of the modification (distortion) can be summarized into following special cases leading to distinct low-energy configurations:

- $\alpha = 45°$, $J_1 > (J_2 + J_2')/2$, ordered AFM phase (as for square lattice)
- $\alpha = \alpha_c > 45°$, $J_1 = (J_2 + J_2')/2$, disordered SL phase
- $\alpha > \alpha_c$, $J_1 < (J_2 + J_2')/2$, ordered FM/line phase

As the proposed modification is "in-plane", lattices with various level of distortion can be fabricated next to each other on one sample (silicon chip), therefore all the lattices will have the same process history. This is much more convenient for scanning through the phase diagram than the z-shifted square lattice, where several samples are needed (one sample → one height shift h).

Similarly to the previous works [15, 28], it is expected that the low-energy configuration of the artificial system will not be perfect realization of the 6 vertex model (type I and II vertices only), therefore local charge defects (type III vertices) can be trapped within the system. In case of being trapped within the SL phase, these charges may be seen as magnetic monopoles (utilizing the dumbbell representation of magnetic moments) [32].

For the DSL new constraint regarding type III vertices emerges from the lattice geometry. When the lattice is distorted ($\alpha > 45°$), vertices that have spins co-directionally aligned with the smaller gap g_1 (see Fig. 2.18) are more likely to occur. In other words, net magnetic moment of type III vertex must be aligned with the smaller gap g_1 (see Fig. 2.19b). Therefore it is possible to divide type III vertices, based on the lattice geometry, into two groups. Favourable vertices (F) that follow this rule (g_1 horizontal → v_9, v_{10}, v_{13}, v_{14}) and unfavourable (NF) that does not follow the rule (v_7, v_8, v_{11}, v_{12}).

To summarize, the main aim of the thesis is to experimentally probe the phase diagram of the 6 vertex model utilizing the DSL geometry. There are three main objectives for this work: 1) reach to a SL phase, 2) observe and analyse trapped magnetic monopoles within the SL phase, 3) determine whether the geometry is suitable to test the theoretical proposal of spin fragmentation [33], that is linked with the monopole density.

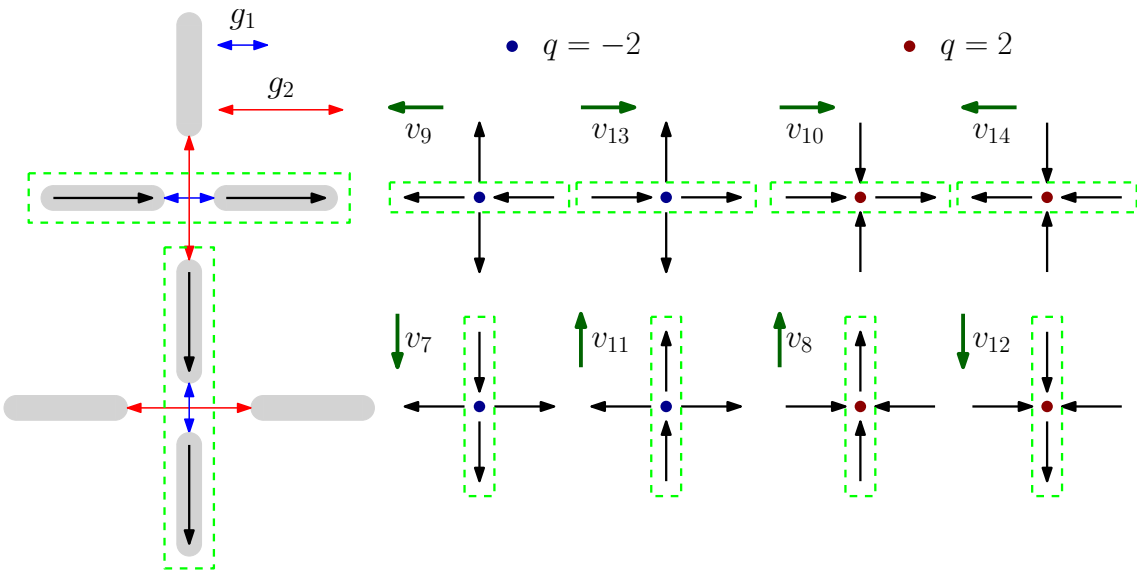

Fig. 2.18: DSL geometry and consequence of the modification on type III vertices. For vertex with horizontal (resp. vertical) gap g_1, vertices with horizontal (resp. vertical) co-directional spins are preferred. Darkgreen arrow represent net magnetic moment of each vertex. Blue (-2) and red (+2) dots visualize "magnetic charge"in the vertex center.

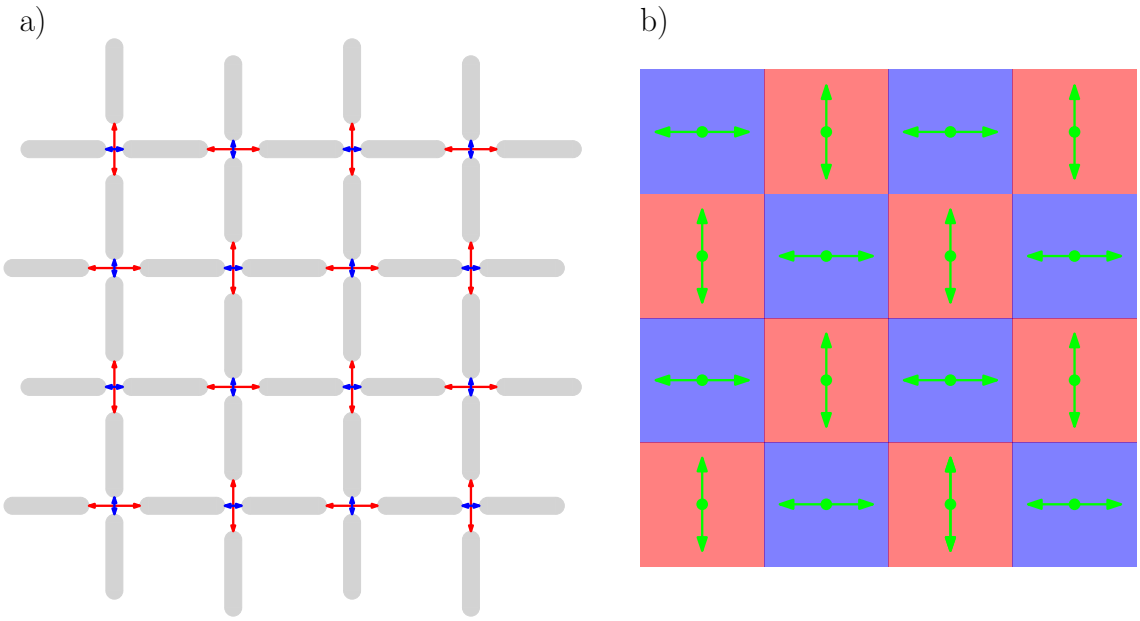

Fig. 2.19: a) DSL system of 4 by 4 vertices. b) Visualization of the type III geometry constraint for this system. Blue (red) squares represents smaller (bigger) gap in horizontal direction, respectively. Green arrow represents preferred direction of net magnetic moment.

3 METHODS

Main purpose of this chapter is to briefly describe methods used in this thesis. The motivation is twofold: 1) prove that the techniques are suitable for this work, 2) describe them separately so the chapter 4 can focus mostly on the results, thus be more compact and "lighter".

3.1 Micromagnetic simulations

Micromagnetic simulations are often used to benchmark ideas and obtain predictions how the system or its modification will behave. These simulations can be linked with experimental realizations through their inputs such as type of the material or geometrical parameters (shape, thickness). Two open acess software solutions for micromagnetic simulations (both based on finite difference discretization method) are available and widely used: OOMMF [34] (cited in almost 2700 publications, several studies related to the problematic [20, 28, 29, 36]) and MuMax^3 [35] (cited by approx. 600 publications, several studies related to the problematic [21, 29]). The advantage of the MuMax^3 software is that it is GPU-accelerated, thus it is much faster than CPU based OOMMF.

In this work MuMax^3 was used to obtain qualitative estimate of how the energy levels (for ground state magnetization) of vertex types evolves with the system modification (distortion). The simulations were designed to mimic the fabricated samples as closely as possible, thus corresponding geometrical parameters and material constants (for permalloy) were used. Magnetic layer thickness was on purpose set to 5 nm (instead of 25 nm for fabricated lattices) to avoid vortex appearance in magnetization. Thus the simulations only provide qualitative estimate of energy levels (previously conducted simulations confirmed that layer thickness alone can not modify arrangement of the energy levels in square lattice [20]).

To illustrate how the simulations were designed, the example of complete input code is provided in Appx A.1. Fig. 3.1 (produced by this input code) visualize how the simulations are conducted. Firstly, the initial geometry and its magnetization is defined (typical cell size of the simulation grid was 1x1x5 nm^3, for the x, y, z respectively). In this case its vertex of DSL geometry (only 1/2 of each magnet is simulated), $w = 150$ nm, $l = 750$ nm, $\alpha = 65°$, $g_1 = 150$ nm and initial magnetization is consistent with type II vertex configuration v_3 – see Fig. 3.1a. Only magnetization close to the outside edge (blue dashed region) is fixed, in other regions it is free to evolve. Initial magnetization in these regions is defined only in rectangular part of the magnet, rounded end is magnetized randomly. Than the energy of the system is minimized and resulting configuration is captured in Fig. 3.1b, it is clear that

magnetization at the rounded edges in the middle of vertex adjusts accordingly to its neighbours. MuMax[3] can also simulate magnetic force microscopy contrast of resulting configuration. Detail focused on the center of the vertex (purple dotted region in Fig. 3.1b) is shown in Fig. 3.1c.

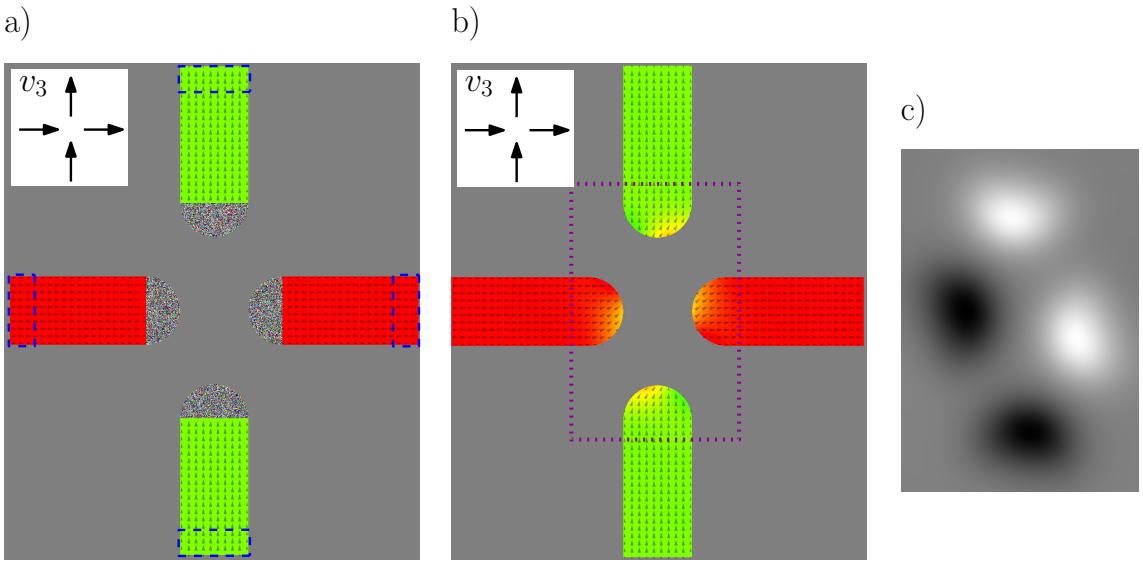

Fig. 3.1: a) Geometry and initial magnetization of type II vertex configuration (v_3 illustrated in the inset). Green (up) and red (right) regions represents direction of magnetization. Blue dashed region indicates area with fixed magnetization (to mimic other half of the magnet), the rounded half-circles are magnetized randomly. b) Resulting ground state magnetization of same vertex. c) Simulated magnetic force image of central region of the vertex – dotted purple region from b). All three images are outputs of the code provided in Appx. A.1.

Total energy of the simulated vertex configuration is also outputted and saved. All experimentally realized lattices (and all possible vertex types) were simulated and the resulting energy levels are presented in Sec. 4.3.

3.2 Sample fabrication

Conventional one-step lift-off process, utilizing electron beam lithography (EBL) and electron beam physical vapour deposition (EBPVD) was used for the sample fabrication. Individual steps of the fabrication process are illustrated in Fig. 3.2. Similar process was previously used for fabrication of artificial spin systems, for example [20, 21, 28, 36].

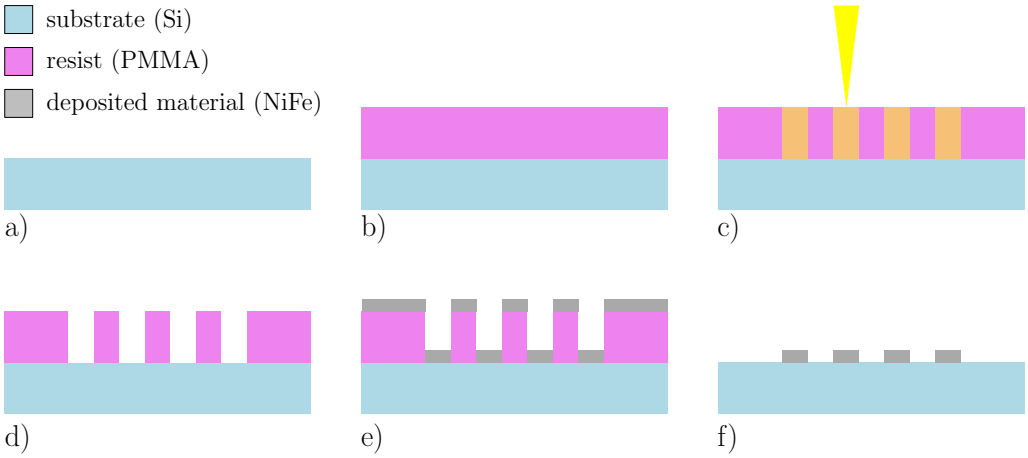

Fig. 3.2: Sample fabrication process: a) suitable substrate is prepared (e.g Si), b) e--beam resist is spin-coated on top (e.g. PMMA), c) resist is exposed by EBL, d) resist (positive in this case) is developed, e) required material is deposited by EBPVD, f) excess material is lifted-off together with the remaining resist.

Sample fabrication for this thesis was conducted by Y. Perrin at Institut NÉEL (Nanofab facility) and CEA (only EBPVD), both in Grenoble. As the used experimental techniques are well-established (and thoroughly described in literature), following subsections are rather brief and aim to emphasize facts relevant to the quality of fabricated structures. SEM images of fabricated structures are provided in Sec. 4.2. Fabrication details are provided in Appx. B.1.

3.2.1 Electron beam lithography

E-beam lithography, combined with other fabrication techniques (such as material deposition, dry-etching etc.), is often used for pattering structures within the sub--micron resolution [37], in fact sub 10 nm resolution was reached [38, 39].

The technique is based on interactions of electron beam with suitable material (e-beam resist). Electron beam modifies local properties of the resist layer, which leads to encoding of the latent image information (see Fig. 3.2c). To obtain the desired structure, the resist must be developed. In case of positive electron resist (e.g.

PMMA), molecules in exposed areas are fragmented, therefore after application of developer dissolve faster than molecules in unexposed areas (see Fig. 3.2d). Thus positive resists are convenient for fabrication of low-dense structures (such as artificial spin systems, typically less than 20 % of the lattice region is covered), because of the lower exposure time.

The quality of the fabrication depends on several factors determined by: e-beam writer/electron microscope itself (primary beam energy, beam spot size etc.), combination of resist/developer (contrast, resolution etc.), strategy of exposure (structure definition, exposure dose etc.) and scattering effects (proximity effect). The fabrication of our artificial spin systems require relatively low-dense binary thin resist mask (see Fig. 3.2d) for following deposition and lift-off, thus scattering effects can be neglected. In our case the final quality of the structures is mostly determined by the profile of the mask (see Fig. 3.3), which is (for given combination of resist and developer) influenced primarily by the exposure dose. Too low dose can lead to missing structures or their parts, slightly lower dose sometimes causes "ears"(Fig. 3.3f) and/or rougher edges. Correct dose leads to ideal profile of resulting structure (sometimes slightly higher dose is used, to prevent "ears"effect). Too high dose can result in lowering the resist thickness, which could affect the lift-off efficiency (commonly used ratio between resist thickness h and deposited material thickness t is 3:1, at least). Therefore it is common practice to sweep the dose by small step (i.e. dose sets of lattices are fabricated), to increase probability of successful fabrication (also used in this thesis).

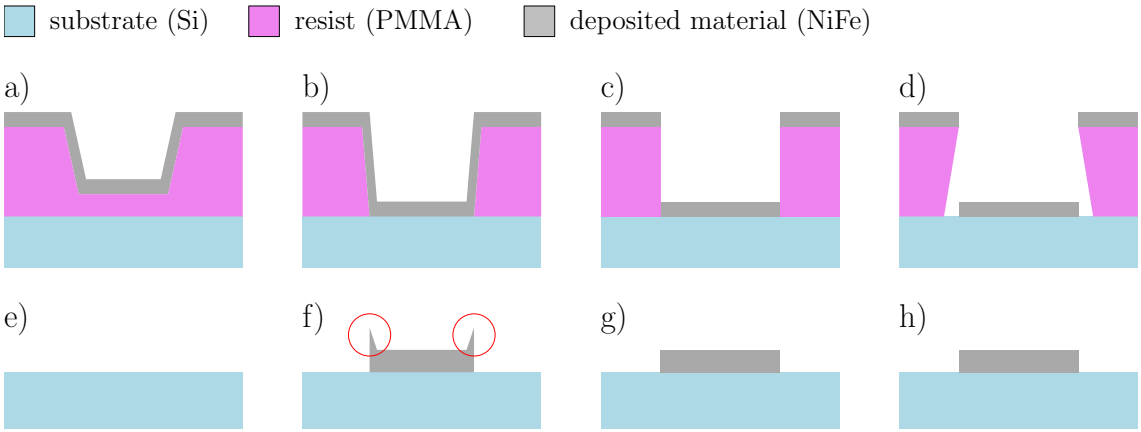

Fig. 3.3: Influence of the dose on the resist profile: a) low dose – undeveloped profile, b) slightly lower dose – moderately underdeveloped profile, c) correct dose – ideal profile d) slightly higher dose – moderately overdeveloped profile. Corresponding resulting structures after lift-off: e) no structure, f) structure have "ears", g), h) ideal structure.

3.2.2 Electron beam physical vapour deposition

Evaporation based techniques are often used within the lift-off process, as they promise somewhat directional deposition because of the high vacuum of the chamber. This effectively reduces the side-wall deposition and usually leads to better results than other techniques (sputtering for example). Different mechanisms of providing the energy to heat/melt the material are used, most commonly direct thermal heating or electron beam.

In this work Electron beam physical vapour deposition [40] (EBPVD) was used. High-energy electron beam is focused on material to be evaporated/deposited, which is placed in the crucible within the vacuum chamber (see Fig. 3.4). The evaporated material then condense on the substrate/sample resulting in formation of deposited layer. To control the deposition rate (resp. layer thickness), EBPVD system is equipped with Quartz crystal micro-balance monitor which uses frequency response of a quartz crystal to estimate the amount of deposited material [41].

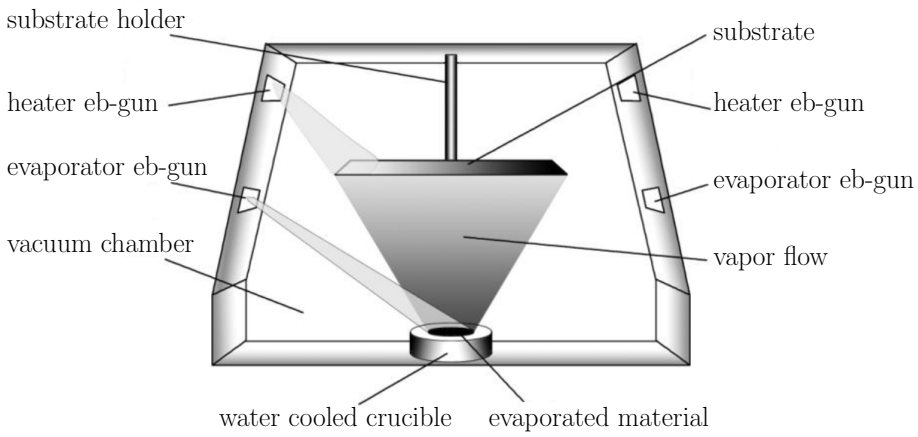

Fig. 3.4: Scheme of electron beam evaporator, adapted from [42].

3.2.3 Lift-off

In order to remove resist mask and excessive deposited material the sample is submerged into a solvent (compatible with used resist). Some solvents can be heated to improve diffusion and dissolving of the resist. To assist separation of excessive deposited material and to prevent its redeposition, the sample is placed face-down into a hour-glass. Next step is to apply short ultrasonic bath treatment, that further improve the separation of residual material. Than the sample is rinced in IPA in order to remove remains of lift-off solvent. Finally, the sample is dried using nitrogen.

3.3 Sample demagnetization

To recover low-energy magnetic configuration of artificial spin system, the sample must be demagnetized. There are two distinct approaches for the demagnetization protocols: field [43–46] and thermal [47, 48]. When designing the artificial spin systems, one must keep in mind what type of demagnetization process is available (and will be used), as the system properties must be adapted (thickness, material etc.) [18]. For our experiment we have chosen the field demagnetization protocol which experimental apparatus is available at Institut NÉEL and was previously used in several works [20, 28, 29, 36]. Therefore the artificial spin systems were designed to be athermal ($t = 25\,\mathrm{nm}$).

In case of field demagnetization protocol, the sample is mounted on a rotating holder, that is placed within the field area. The sample is positioned in a way, that the applied external magnetic field is in-plane (with the nanomagnets). Usually, ac demagnetization field (sinusoidal shape) modulated by linear decreasing function is used (see Fig. 3.5). The initial field (B_{max}) is set up well above the coercive field of the system elements (magnets). Therefore, until the time t_1 is reached all the

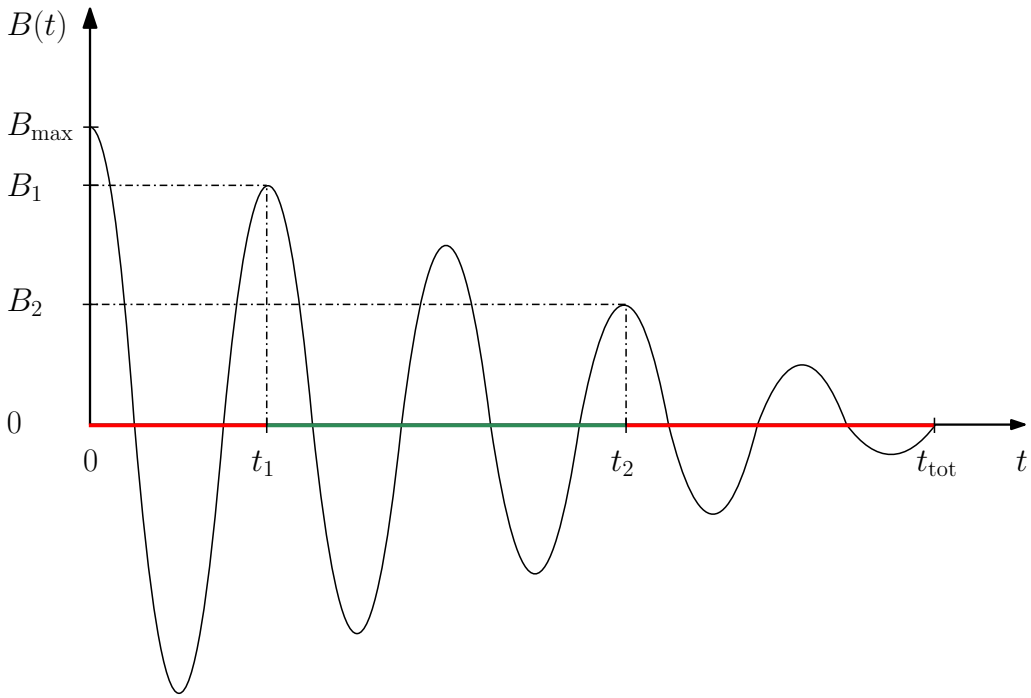

Fig. 3.5: Scheme of ac field demagnetization protocol, the effective zone is illustrated by the green line.

magnets are flipping to align with the external field and no demagnetization is conducted. When the time t_1 is reached the applied field is no longer strong enough to force all magnets to align with the field and only spin-flips that leads to lowering

the total energy of the system are performed. After the time t_2 is reached the external field is too low to reverse any magnet and the final configuration is reached. Nice demonstration of field demagnetization process is provided in Supplementary information of Perrin et. al. [28], in form of video.

The efficiency of the demagnetization process is mostly determined by the length of effective zone (from t_1 to t_2). Generally, longer effective zone leads to better demagnetized samples (closer to the low-temperature configuration), but the demagnetization dynamics prevents reaching of perfect ground-state configuration (in most artificial systems). Thus increasing the length of demagnetization process will not lead to a better demagnetized samples after some limit is reached.

The photo of the experimental apparatus used in this work is provided in Fig. 3.6. In the experiment only the length/duration of demagnetization process was changed (reduced from 148 h to 72 h). The other parameters (initial field size, frequency of the ac field and RPM of the holder) were always set to the same values: $B_{\mathrm{max}} = 100\,\mathrm{mT}$, $f_{\mathrm{field}} = 250\,\mathrm{mHz}$, $f_{\mathrm{holder}} = 1200$ RPM. Therefore the sample rotation (frequency) is much faster than the field alternation. To check that the initial value of magnetic field (B_{max}) is sufficient, the regular square lattice was saturated in (11) direction by this field, which lead to perfect alignment of all magnets (Fig. 3.8a), thus the initial field is strong enough.

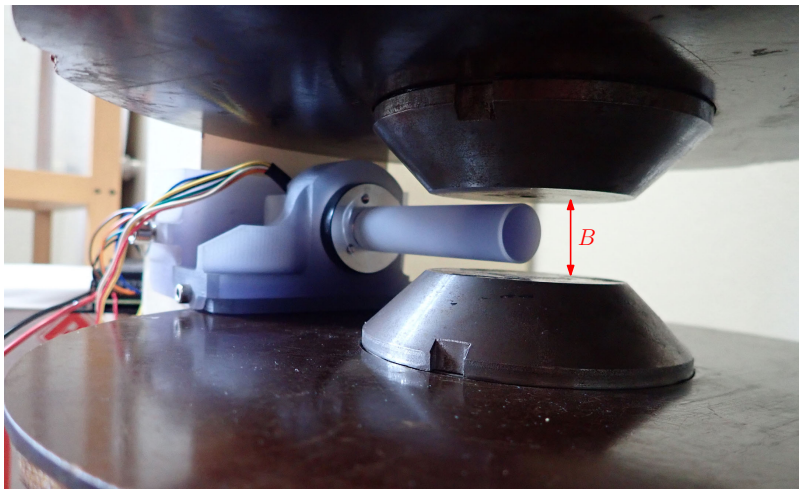

Fig. 3.6: Experimental apparatus for demagnetization protocol. The sample is attached to the end of the rotating plastic rod, which is placed within the field area.

To determine whether the demagnetization process was efficient, regular square lattice may be used. If the captured magnetic configuration is close to expected ground-state (only type I vertices), the demagnetization protocol may be considered effective. Example of MFM images of saturated (as when demagnetization protocol starts, Fig. 3.8a) and demagnetized (Fig. 3.8b) regular square lattice is provided.

3.4 Magnetic imaging

Several magnetic imaging techniques can be used to characterize magnetic configuration of artificial spin system directly in real space, e.g Magnetic force microscopy (MFM), Photoelectron emission microscopy (PEEM) or Lorentz transmission electron microscopy (LTEM) [17]. Based on magnetic imaging technique to be used in experiment, the design of artificial spin systems should be optimized/adapted, similar as with demagnetization protocol. In our experiment we choose MFM, as the technique is available (and well developed) at Institut NÉEL and was sucesfuly used in previous works [20, 28, 29, 36]. The thickness of fabricated magnets ($t = 25\,\mathrm{nm}$) should be enough to provide sufficient magnetic contrast, when imaged by the MFM technique.

3.4.1 Magnetic force microscopy

Magnetic force microscopy (MFM) is a magnetic imaging technique derived from the atomic force microscopy (AFM). Both techniques belongs to the family of scanning probe microscopy techniques. As the name suggests, the main idea behind these techniques is to characterize properties of the sample by scanning some probe over the sample. The information itself is then deduced from the interaction between the probe and the sample. As both techniques (AFM – 1986 [49], MFM – 1987 [50]) were introduced more than 30 years ago, they are nowadays well-established and described in the literature (e.g. educational SPM manual [51], MFM review paper mentioning artificial spin systems [52]). Therefore only brief description of the techniques (and their application for measurement of artificial spin systems) is provided.

MFM enables measurement of interaction between the probe (with magnetic coating) and stray field emerging from the sample. From the stray field it is possible to deduce the distribution of magnetization within the sample. To separate the magnetic component of the force interaction (tip-sample) the two-pass oscillatory method is used (see Fig. 3.7). The first pass (Fig. 3.7a) utilizes the tapping mode (tip is oscillated at a frequency close to the resonance) and the sample topography (Fig. 3.7c) is recorded. Therefore the first pass is equivalent to an AFM scan. During the second pass (Fig. 3.7b) the tip shadows the topography of the sample (recorded in the first pass) with constant height offset h (set by operator), therefore the tip-surface distance is constant and the tip-sample interaction is dominated by magnetic force. As the tip/cantilever is also oscillated during the second pass, the MFM image is obtained by recording the changes of the amplitude or the phase. If the tip is repelled (resp. attracted) by the sample the phase shift is positive (resp. negative) [51], this is illustrated by the Fig. 3.7b,d).

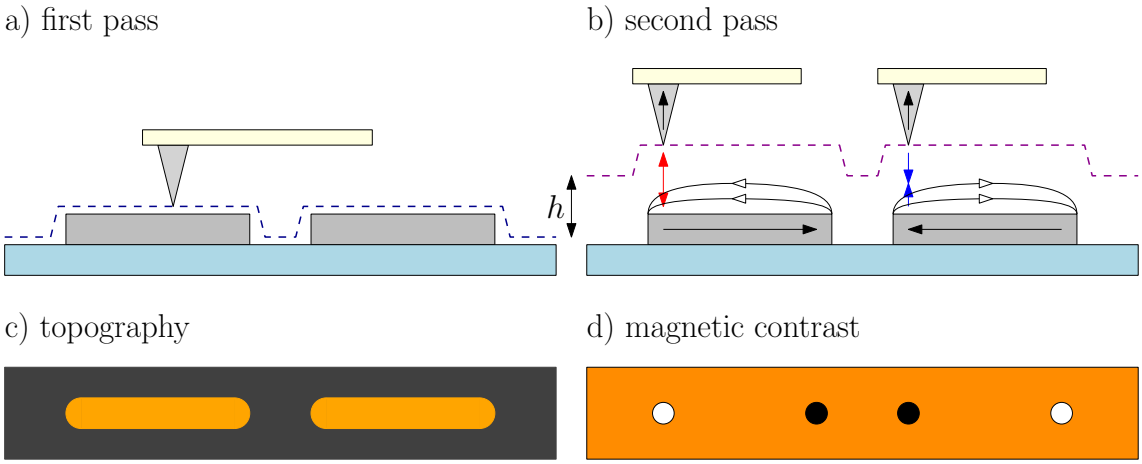

Fig. 3.7: a) Illustration of first pass, which records the topography. Blue dashed line represents trajectory of the tip. b) Illustration of the second pass, which records the magnetic information. The tip with magnetic coating (arrow represent its moment) follows the trajectory recorded in (a) with height shift h, trajectory is represented by magenta dashed line. Based on magnetization of the elements (black arrows), the tip is either attracted (blue arrow) or repelled (red arrow). c) Visualisation of ideal topography scan of two magnets. d) Visualisation of ideal magnetic contrast image obtained for two magnets, magnetization consistent with (b). Gwyddion [53] color scale is mimicked: white (resp. black) represents positive (resp. negative) phase shift, orange represents no phase shift (background, non-magnetic).

3.4.2 Measurement details

The magnetic imaging was conducted at Institut NÉEL (AFM-STM platform) utilizing *NT-MDT Ntegra* microscope. In-house prepared magnetic tips with thickness of magnetic coating (CoCr alloy) ranging from 30 to 75 nm were used as probes. MFM two-pass oscillatory method (described above) was used. Typical lift height h of second pass was 50 – 100 nm.

As the purpose of the magnetic imaging in this work is to resolve the spin configuration of the system, the scanning parameters were optimized to obtain recognizable image within the shortest possible time (approx. 20 min per lattice). Typical values of scanning parameters (tuned based on the lattice size) are provided below:

- Scan size: 25x25 – 38x38 µm
- Data points (resp. number of lines): 512 – 800
- Scanning frequency: 0.4 – 0.5 Hz

The lattices were always oriented the same way and the same scanning pattern (horizontal: left to right, vertical: top to bottom) was used. Example of topography and magnetic images acquired by the two-pass MFM is provided in Fig. 3.8.

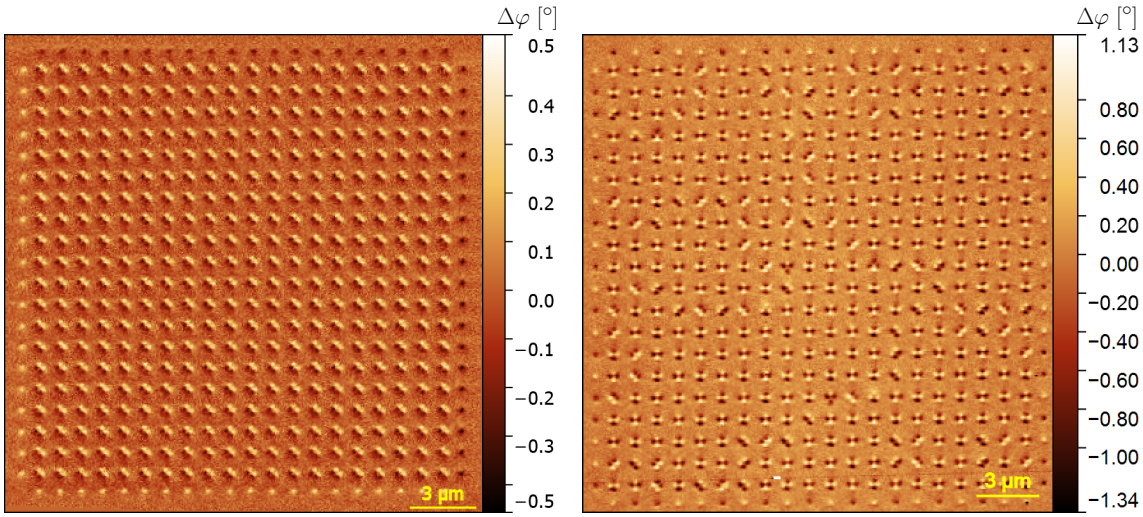

(a) MFM, saturated (11) direction

(b) MFM, demagnetized (148 h)

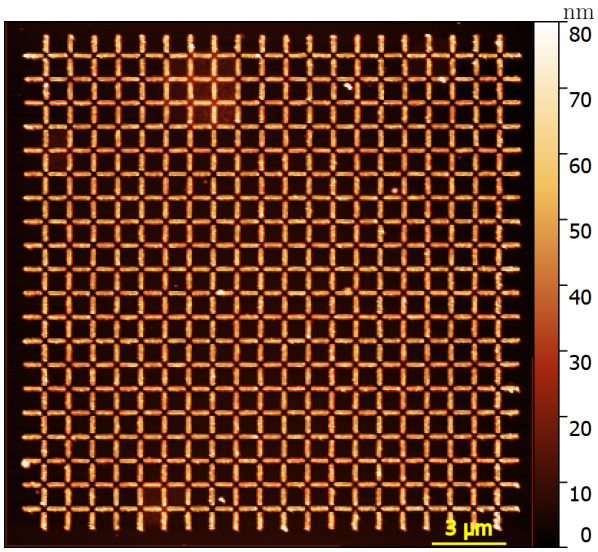

(c) AFM, overall topography image

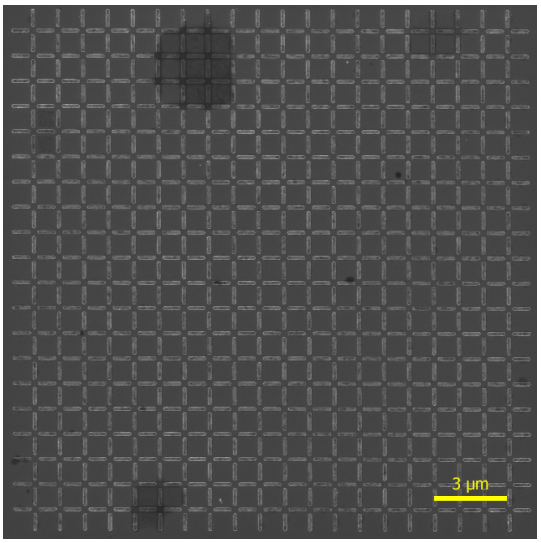

(d) SEM, overall image

Fig. 3.8: SEM and AFM/MFM images of fabricated regular square lattice: $\alpha = 45°$, $g_1 = 300\,\text{nm}$, dose 5, demag 148 h (1).

Above presented Fig. 3.8 illustrates several facts. Firstly, the subfig. a) verifies that the initial field of demagnetization protocol is strong enough, the image was obtained by saturating the sample in (11) direction in the experimental apparatus for demagnetization process. As the demagnetization process starts with this field the subfig. a) may be seen as magnetic configuration at the start of the process. The subfig. b) shows the magnetic image after the demagnetization process, thus we can directly compare before/after images. Also subfig. a), b) reveal that all magnets are single-domain. Subfig. c) shows that even topography recorded by "speed-optimized"AFM scan (approx. 3 – 4 data points per magnet width) captures the lattice geometry somewhat authentically (except the magnet height which is overstated).

3.5 Analysis of measured data

Y. Perrin developed toolkit (*Perrin toolkit*) for analysis of artificial spin systems based on square lattice geometry, when working on z-shifted square lattice during his doctoral studies [20]. This toolkit requires spin-configuration as an input. It is possible to evaluate the lattice manually (from the MFM image), but it is rather time-consuming as each individual spin must be resolved (typical lattice used in this work has 840 spins and manual evaluation takes approx. 90 min). Therefore I developed semi-automatic evaluation MATLAB script that enables extraction of spin (resp. vertex) configuration in more friendly manner and in shorter time (approx. 20 min per lattice). The script is accompanied by another analysis toolkit, that provides additional information (*Brunn toolkit*). How the codes work together (and their inputs/outputs) is illustrated in Fig. 3.9.

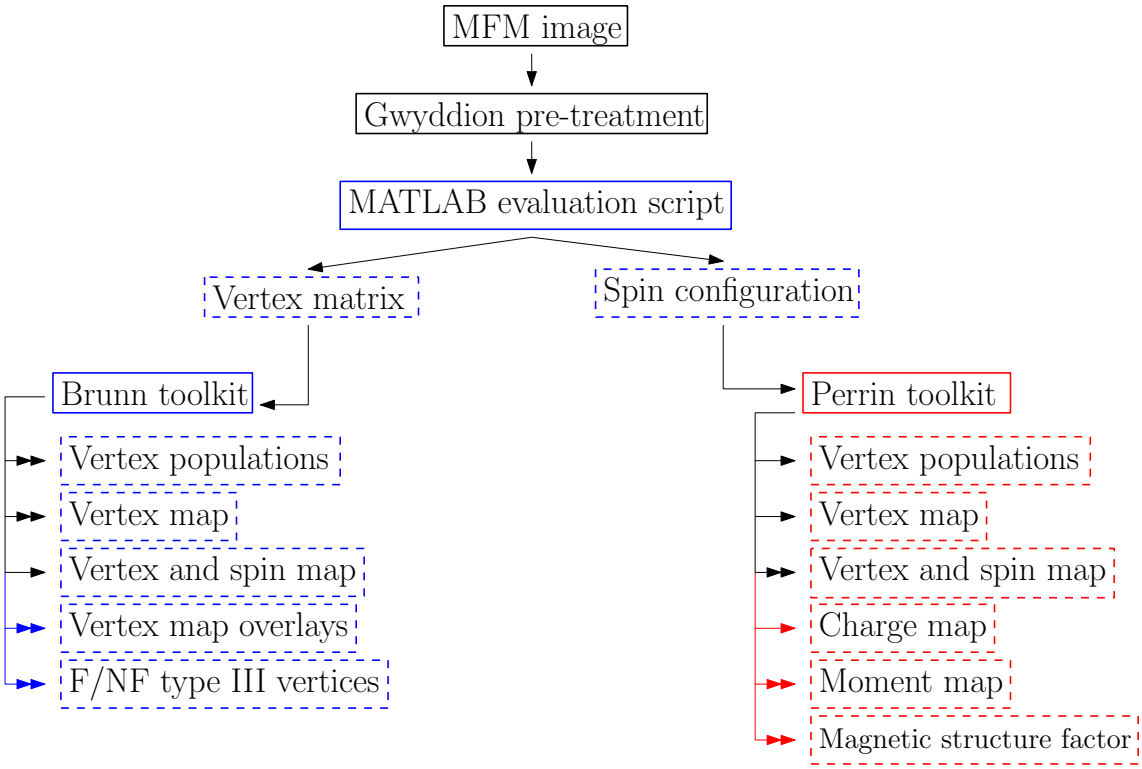

Fig. 3.9: Diagram of analysis steps. Blue (resp. red) frames represent code developed by author (resp. Y. Perrin), dashed frames represent outputs. Double-arrows represent outputs used in this work, blue (resp. red) arrows represent unique output for given toolkit.

Important steps of analysis and key outputs are described in following subsections. Other (mostly derived) outputs are presented in Chap. 4 with intuitive description/introduction.

3.5.1 Pre-treatment

Pre-treatment of measured MFM images is conducted in open source SPM data visualisation and analysis software Gwyddion [53]. The main goal of this step is to obtain image of magnetic contrast, that is later used as input for evaluation script. As we are not interested in quantitative analysis of the image, any operation that leads to higher contrast/better image quality can be used. Typical data operations were: level data by mean plane, align rows (either matching or median method), rotation and distortion correction, cropping and manually setting the color range (to optimize contrast).

3.5.2 Configuration extraction

To speed-up and facilitate evaluation/extraction of spin configuration from magnetic image the MATLAB evaluation script was created. Unlike the *Image automatic analysis software* (IAAS) created by V. Schánilec [21] for kagome geometry (3 magnets are meeting at vertex point, 8 possible vertex configurations), my evaluation script requires manual evaluation of vertices. But as the evaluation is assisted by the code, it is much easier and faster than evaluate the configuration manually. The script assisted evaluation can be break-down to individual steps:

1. **MFM image import** – User selects pre-treated MFM bitmap image.
2. **Marking lines/rows of MFM image** – User marks all 4 lattice borders and first row and column (see Fig. 3.10a), than the vertex grid (how the image will be cropped) is shown (see Fig. 3.10b).
3. **Evaluation of borders** – Based on previous step, the lattice borders are extracted and user is asked to evaluate them (b key for black dot, v key for white dot).
4. **Evaluation of vertices** – Based on second step, the image is cropped to individual vertex images and 3x3 vertex images. User is asked to evaluate each individual vertex by pressing corresponding key (see Fig. 3.10c). The 3x3 vertex image shows neighbouring vertices, thus assist the decision. If some vertex is not recognizable, user press x key.
5. **Vertex and spin map check** – To provide user with direct feedback, the vertex and spin map is plotted (see Fig. 3.10d). The main purpose of this step is to check that there are no mistakes in evaluation of vertices. As each spin is defined from two neighbouring vertices, three outcomes are possible: agreement (spin is plotted either blue or red), conflict (spin is not plotted) or spin is defined only by 1 vertex as the other is not recognizable (spin is plotted green). The user than manually corrects undefined spins.

6. **Export of vertex matrix, spin configuration** – Next step is to export vertex matrix and spin configuration, both to archive and to use for next procedures. These outputs are exported to a .txt file.
7. **Final output generation** – Final step is to generate desired outputs, typically the basic range of outputs includes: vertex populations (.txt), vertex and spin map (image), calculated magnetic structure factor (image). The direct outputs (included in *Brunn toolkit*) are created/saved immediately, indirect outputs (processed by *Perrin toolkit*) can be automatically generated by running batch file, that triggers required scripts.

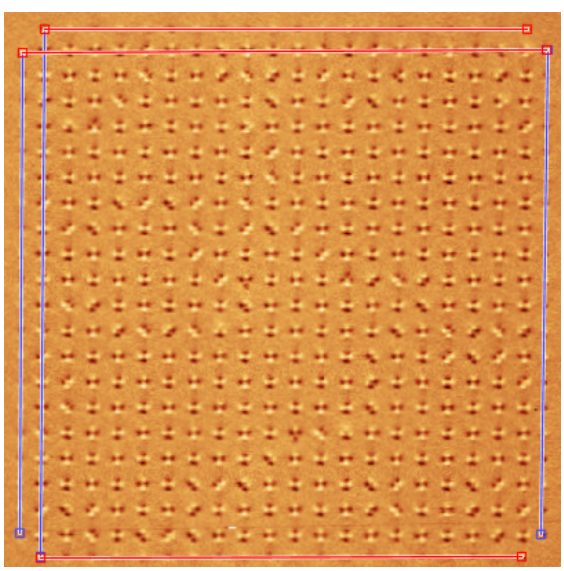

(a) User marked borders and first row/column

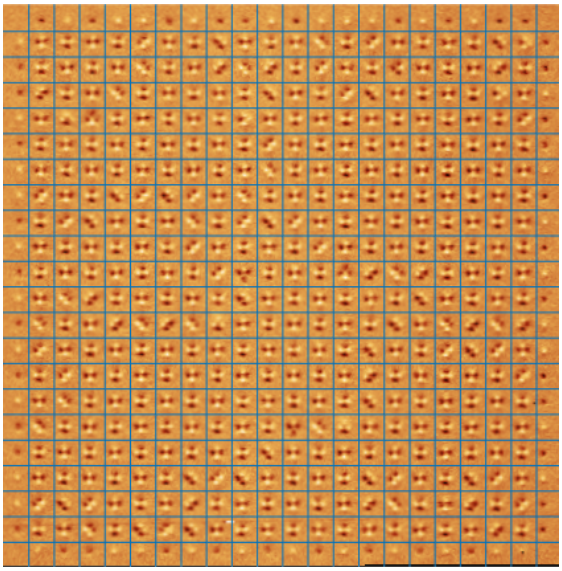

(b) Vertex grid based on (a)

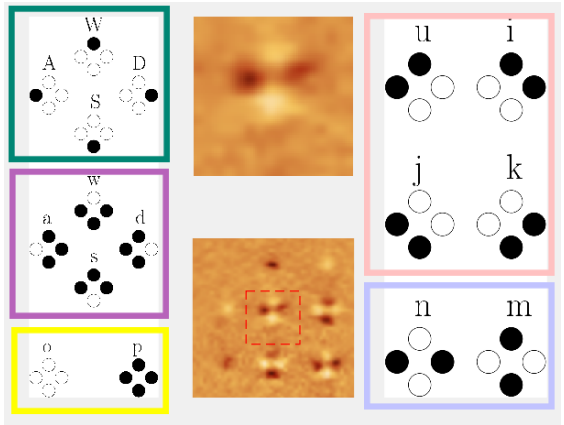

(c) Vertex evaluation GUI

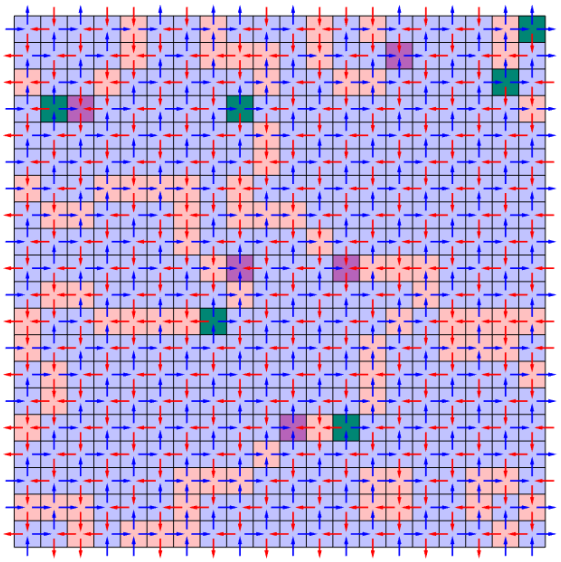

(d) Vertex and spin map

Fig. 3.10: Illustration of main steps of MATLAB evaluation script for regular square lattice: $\alpha = 45°$, $g_1 = 300\,\mathrm{nm}$, dose 5, demag 148 h (1).

It is worth to discuss more closely Fig. 3.10c,d to ensure that the transition from MFM image to vertex (resp. spin) configuration is described properly. Each vertex is defined by 4 circles (poles) that can be either black or white. The spin for each magnet is assigned (consistent with Fig. 3.7b,d) as arrow pointing from white pole to black pole, therefore we can use either arrow or pole representation (both illustrated in Fig. 3.11 for various vertex types).

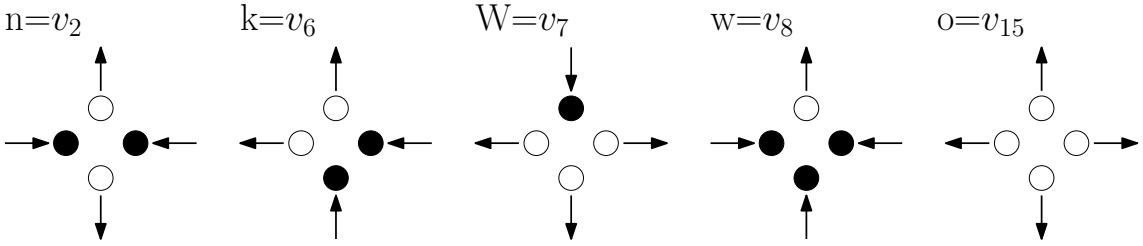

Fig. 3.11: Equivalence of dot representation (that mimics MFM contrast) and arrow representation (introduced in Fig. 2.8) for different vertices.

When plotting the vertex map in subfig. d) each vertex is represented by coloured square (colours are illustrated in subfig. c) by the frames): type I vertices are blue, type II are red, type III $g = -2/g = +2$ are darkgreen/magenta, and type IV are yellow. Spins are plotted on top of the vertex map to provide additional information, blue (resp. red) spins corresponds to spins oriented along (resp. against) x, y direction.

To summarize, the MATLAB evaluation script provides faster configuration extraction than the manual analysis. It is also almost "mistake-proof"as each direction of each spin is derived from both ends (thus two times). Another benefit is that consecutive analysis procedures/scripts can be started automatically, when the spin configuration is extracted. Experienced user can therefore analyse one lattice (20 x 20 vertices) in approx. 20 minutes. The evaluation could be speeded up even more, if only each second vertex (chequerboard pattern) would be evaluated. We would lost the double information about each spin, but the process could be shortened to almost half the time.

Naturally, one may recommend to automatize the evaluation process via image recognition techniques. In fact, the artificial spin systems are very good candidate as each spin can point only in two directions (up/down, resp. left/right), thus can be effectively described by Ising like variable. Same statement is valid for elementary objects of interest in MFM contrast, either white or black pole is present. As more than 60 000 different individual vertex images were manually characterized in this work, I would be tempted to try to use them as learning/validation set for some automatic algorithm in the future.

3.5.3 Vertex and spin mapping

In Fig. 3.10d vertex and spin map generated by the *Brunn toolkit* was presented. It is also possible to obtain similar output when *Perrin toolkit* is used. Comparison of these outputs is provided in Fig. 3.12.

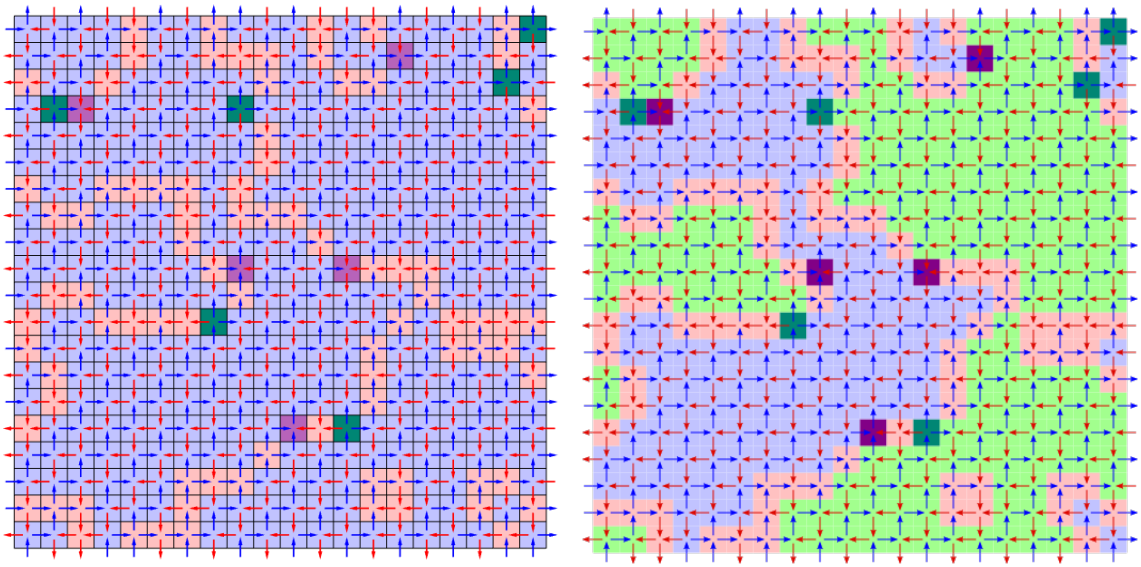

(a) *Brunn toolkit* (b) *Perrin toolkit*

Fig. 3.12: Comparison of vertex and spin mapping for regular square lattice: $\alpha = 45°$, $g_1 = 300\,\text{nm}$, dose 5, demag 148 h (1).

Main difference between these two outputs is that map generated by *Perrin toolkit* distinguishes separated type I patches by two colours – lightblue and light-green, because of this functionality (and slightly better visual appearance) all the configuration mapping will be done by *Perrin toolkit*, when possible.

3.5.4 Magnetic structure factor

The magnetic structure factor (MSF) is a convenient tool to characterize the spin configuration of an artificial spin system, and is often used – e.g. [21, 28–30]. MSF is numerically calculated as a Fourier transform of pairwise spin correlations (derived from the measured spin configuration) [18]. The output of this operation provides magnetic diffraction pattern (as in neutron diffraction experiments), which nicely visualize order/disorder of the system [18].

As in this work MSF is calculated by *Perrin toolkit*, only resulting magnetic diffraction pattern and their properties are discussed bellow. Thorough description of how the MSF is calculated is provided in Y. Perrin's Ph.D. thesis [20], less comprehensive in Methods of this paper [28]. Nice example of how the MSF is "vertex type distribution sensitive"is provided in this review [18].

Fig.3.13 illustrates typical magnetic diffraction patterns obtained for different magnetic configurations of square spin system (20x20 vertices).

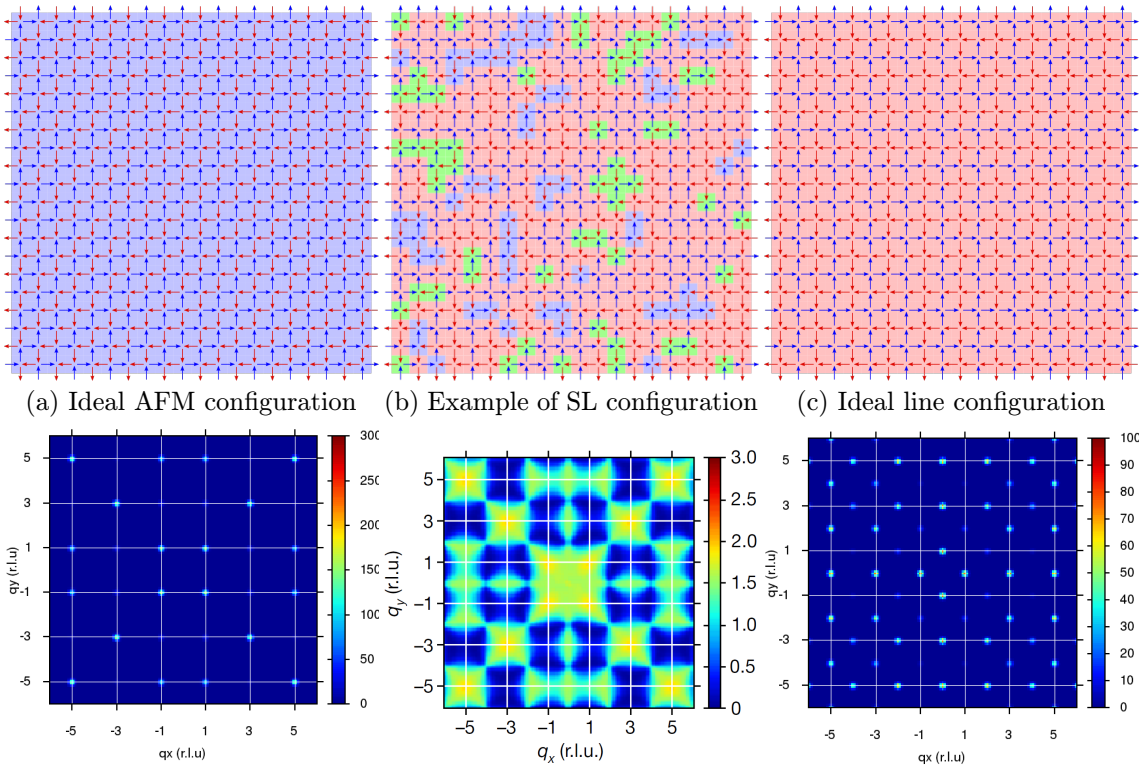

(a) Ideal AFM configuration (b) Example of SL configuration (c) Ideal line configuration

(d) MSF of (a) (e) Ideal MSF of SL phase (f) MSF of (c)

Fig. 3.13: Magnetic configurations of square spin system: a) Ideal AFM ground-state configuration (only type I), b) Example of spin-liquid like configuration (mixture of type I and II), c) Ideal line configuration (only type II). For a) and c) associated magnetic structure factors (MSF) are provided in d) and f), respectively. Both MSF reveal clear magnetic Bragg peaks. e) Illustrates ideal MSF of spin-liquid phase, taken from [20], the MSF reveals characteristic diffused but structured background.

If the magnetic configuration is ordered, the magnetic structure factor consist of strong Bragg peaks. Fig. 3.13 shows perfectly ordered AFM phase and line phase, therefore the Bragg peaks in associated MSF have strong intensity. If there are some imperfections, the intensity of these peaks start to be blurred (and loose on intensity).

Subfig. e) shows ideal magnetic structure factor obtained by averaging many SL simulated configurations. In this case no Bragg peaks are present and the MSF consist of characteristically structured diffused background of disordered liquid-like phase. If there is some order left, we may see less even distribution of intensity and more intense peak can emerge.

4 DISTORTED SQUARE LATTICE

4.1 Sample overview

To experimentally probe the properties of DSL spin system, following lattices were designed, fabricated and studied. Two sets, each of 7 lattices, were fabricated for basic gap $g_1 = 300\,\text{nm}$ and $g_1 = 150\,\text{nm}$. Within each set, lattices differ by angle α (see Tab. 4.1), therefore first lattice is regular square lattice ($\alpha = 45°$) and others have various level of distortion. Other geometrical parameters were same for both sets: $L = 750\,\text{nm}$, $w = 150\,\text{nm}$, $t = 25\,\text{nm}$ NiFe + 3 nm Al. Geometrical parameters are illustrated in Fig. 4.1a. Typical size of the system for each lattice was 20 by 20 vertices (Fig. 4.1b shows system of 4 by 4 vertices).

Tab. 4.1: Overview of parameters for two sets of DSL systems.

α [°]	g_1 [nm]	g_2 [nm]	g_2/g_1 []	α [°]	g_1 [nm]	g_2 [nm]	g_2/g_1 []
45	300	300	1.00	45	150	150	1.00
50	300	358	1.19	50	150	179	1.19
55	300	428	1.43	55	150	214	1.43
60	300	520	1.73	60	150	260	1.73
65	300	643	2.14	65	150	322	2.14
70	300	824	2.75	70	150	412	2.75
75	300	1120	3.73	75	150	560	3.73

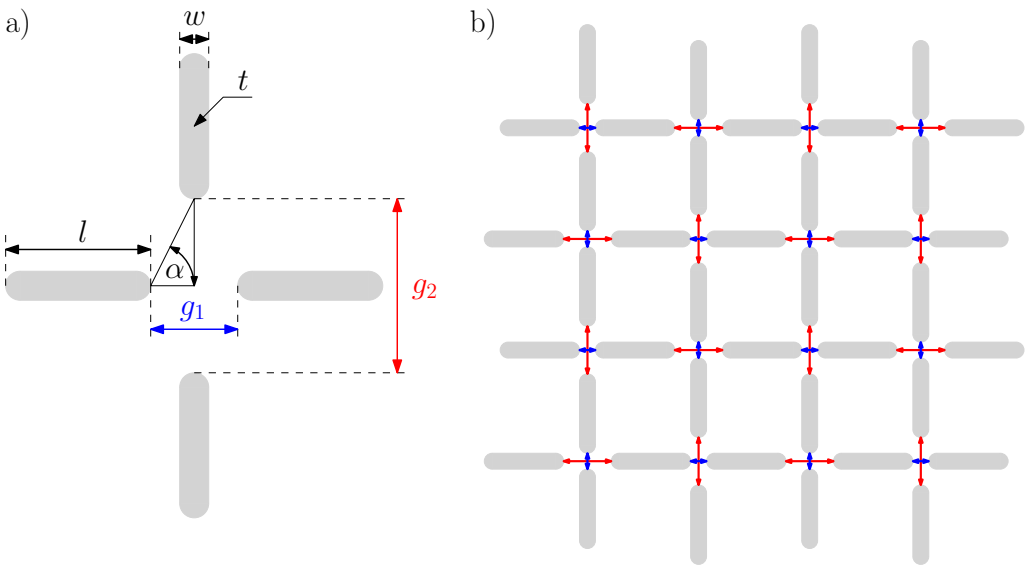

Fig. 4.1: a) Geometrical parameters of DSL geometry. b) DSL system of 4 by 4 vertices.

4.2 Results of fabrication

In previous section we described the range of studied lattices (2 sets, 7 lattices each). Let's call these 14 lattices geometry package. During the EBL this package was patterned 5 times with varying exposure dose (from 240 $\mu C/cm^2$ to 320 $\mu C/cm^2$, with step of 20 $\mu C/cm^2$). For the ease of description we will refer to them as dose 1 (d1, lowest) to dose 5 (d5, highest). Therefore each lattice on the sample can be precisely described by three parameters: g_1, α and dose.

First step to determine quality of the fabrication is to verify, that all elements of pattern were transferred onto the sample. This condition is met by all d4 and d5 lattices. In case of d3, based on lattice density some magnets are missing. Therefore we will mainly focus on d4 and d5 lattices, which provide us with 28 lattices in total (all with system size at least 20x20 vertices). SEM images of d5, $g_1 = 300$ nm lattices are provided in Fig. 4.2.

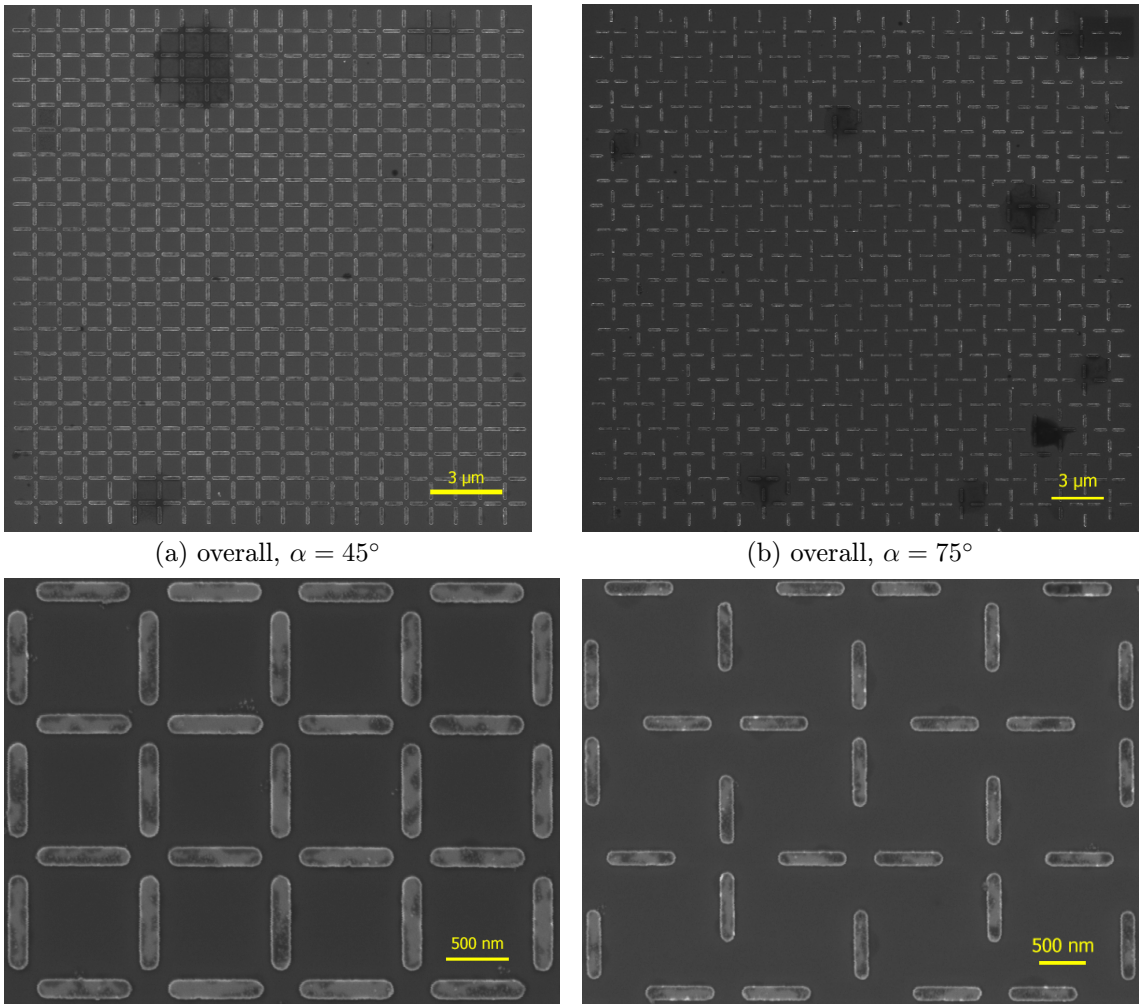

(a) overall, $\alpha = 45°$

(b) overall, $\alpha = 75°$

(c) detail, $\alpha = 45°$

(d) detail, $\alpha = 75°$

Fig. 4.2: SEM images of fabricated lattices: $g_1 = 300$ nm, dose 5.

Next step of assessing the quality of the fabrication is to determine how well are the elements (magnets) patterned. It is expected that this will be also dose dependant. In our sample the best patterning quality is achieved for highest dose (d5), therefore d5 lattices will be our first choice. In fact, the pattering quality influence the properties of the system rather significantly and will be discussed in detail later (Ssec. 4.4.6).

4.3 Results of micromagnetic simulations

As the simulations were conducted after the fabrication, the main goal was to mimic the fabricated geometry. Also the simulations were conducted for lower thickness of the magnetic layer ($t_{\mathrm{sim}} = 5\,\mathrm{nm}$, $t_{\mathrm{exp}} = 25\,\mathrm{nm}$,), so we must perceive them as qualitative estimate only. Details on designing the micromagentic simulations are provided in 3.1.

Fig. 4.3 shows results of the simulations for lattices with gap $g_1 = 300\,\mathrm{nm}$. Total energy of each vertex (sum of magnetostatic and exchange energy) is normalized to the energy of non-distorted type I vertex ($g_2/g_1 = 1$, $\tan(\alpha) = g_2/g_1$).

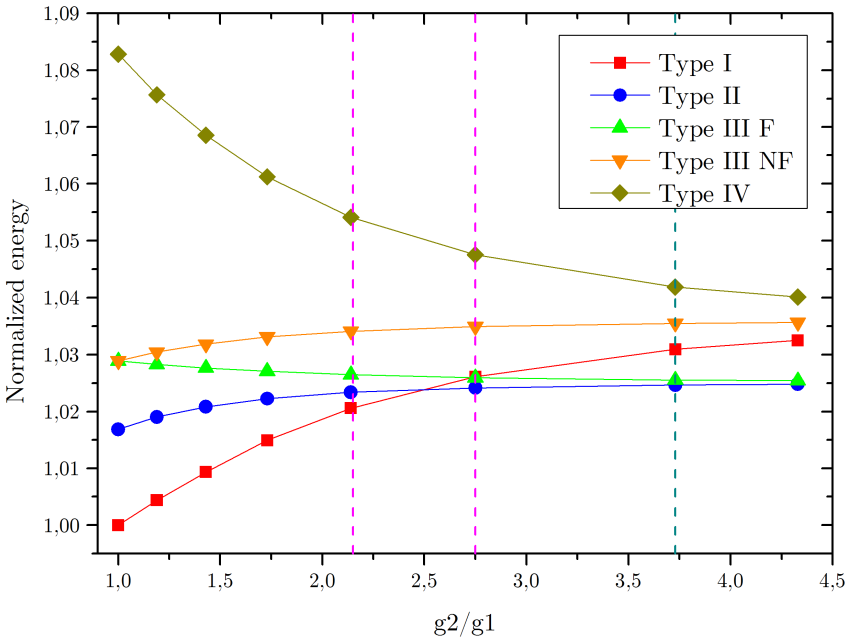

Fig. 4.3: The total normalized energy of vertex types with respect to the distortion of the lattice, $g_1 = 300\,\mathrm{nm}$.

Closer look at Fig. 4.3 reveals how the distortion modifies the energy levels of the vertex types. For the first lattice – regular (non-distorted) square lattice ($g_2/g_1 = 1$), we recognize 4 distinct energy levels as described by 16 vertex model (Ssec. 2.2.1,

Eq. 2.2), as expected the energy increase from type I to type IV. Type III F (resp. NF) stands for favourable (resp. unfavourable) alignment of net vertex moment with respect to the geometry (see Fig. 2.18). In case of regular square lattice we expect them to be equal in energy, which corresponds with the result of the simulation.

With increasing distortion the energy gap between type I and type II is reduced to a point where they intersect. Here we expect the true degeneracy of 6 vertex model which should lead to the disordered SL phase (magenta dashed lines represents area of interest for SL phase, between 5th and 6th lattice). We also see that with increasing distortion the energy level of type III splits as expected (thus F configuration is lower in energy than NF). To estimate further influence of distortion one more lattice (right to dashed lightblue line, 8th data point) with maximum distortion allowed by the size of simulation world was added. We see that energy of type I further increase and in a "big-distortion"limit we can expect that the configuration will be dominated by type II and type III F vertices. The energy of type IV decrease but still remains the highest within the system.

Similar trends can be observed for the lattice with gap $g_1 = 150\,\mathrm{nm}$ (see Fig. 4.4). The intersection of type I and type II energy is slightly displaced towards more distorted lattice (represented by the magenta dashed line), therefore we can expect the SL phase for the 6th lattice. The "high-distortion"limit (behind dashed lightblue line, 8th data point) also show similar behaviour.

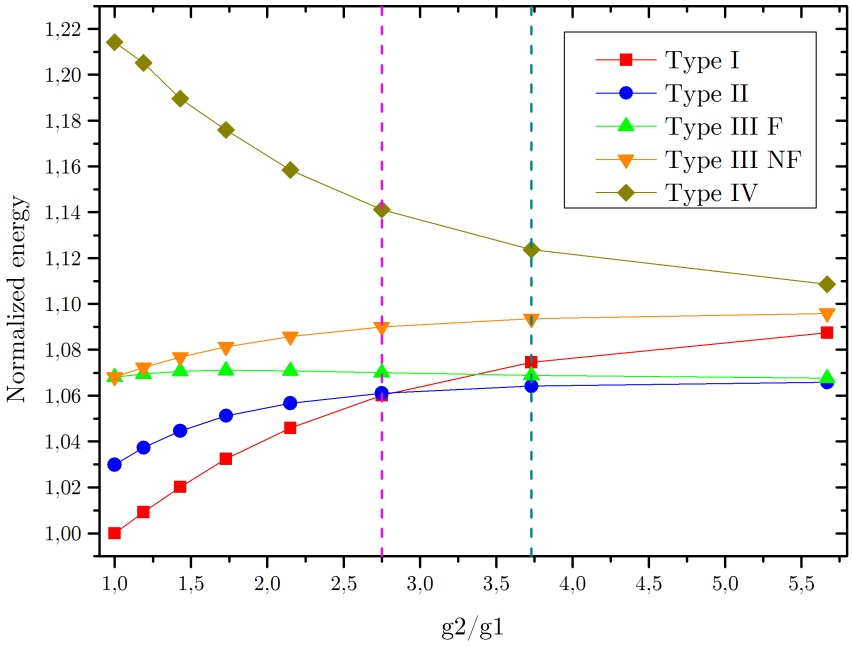

Fig. 4.4: The total normalized energy of vertex types with respect to the distortion of the lattice, $g_1 = 150\,\mathrm{nm}$.

When comparing the simulated energy levels of regular square lattice for $g_1 =$

300 nm and $g_1 = 150$ nm, it is visible that for smaller gap the energy levels are more distant (e.g. energy difference between type I and type II). Therefore it would be reasonable to expect that with smaller gap, we should achieve more ordered ground--state like configuration (only type I). Later we will show, that it is in fact quite the opposite (see Ssec. 4.4.7).

To conclude, the micromagnetic simulations support the proposed idea, that with various distortion we modify the energy levels of vertex types. Most notably, with proper critical distortion we should be able to reach the true degeneracy of the 6 vertex model (i.e. ice model) and observe disordered SL phase.

4.4 Probing the phase diagram of DSL system

In previous section we have provided qualitative estimate of how the distortion affects the energy levels of the 16 vertex model, therefore it also influences the low-energy magnetic configuration of the system. To bring the lattices into their low-energy states we used field demagnetization protocol (details provided in Sec. 3.3). After that the lattices were imaged by magnetic force microscopy (see Sec. 3.4) and their spin configurations extracted and analysed (see Sec. 3.5). This process (demag $\rightarrow$ mfm $\rightarrow$ analysis) was repeated several times. As all the lattices are on the same chip, we can be sure, that the demagnetization (field) history is same for all of them. Therefore we can compare their magnetic configurations directly and observe influence of the distortion. For sake of completeness we provide overview of which sets of lattices (dose 5, $g_1 = 300$ nm is referred to as d5g300 etc.) were measured after which demagnetization protocol. After first two demagnetization protocols, 148 h (1) and 72 h (2), it was determined that 72 h long demagnetization protocol is sufficient enough (as they perform similarly – see Fig. 4.5a,b).

Tab. 4.2: Overview of demagnetization protocols and following measurements of lattice sets.

demag protocol	d5g300	d4g300	d5g150	d4 g150	d3g300	d3g150
148 h (1)	√	√	√	√		
72 h (2)	√	√	√	√		
72 h (3)	√	√				
72 h (4)	√	√	√	√	√	√
72 h (5)	√	√	√	√	√	√
set measured	5x	5x	4x	4x	2x	2x

4.4.1 Demagnetization efficiency assessment

Firstly, we need to determine whether the demagnetization process was efficient in minimizing the system energy. To determine the quality of demagnetization the regular square lattice (d5g300) will be used as reference lattice. We expect ground--state like AFM configuration dominated by type I vertices. The resulting reference lattice configurations for all 5 demagnetization protocols are provided in Fig. 4.5.

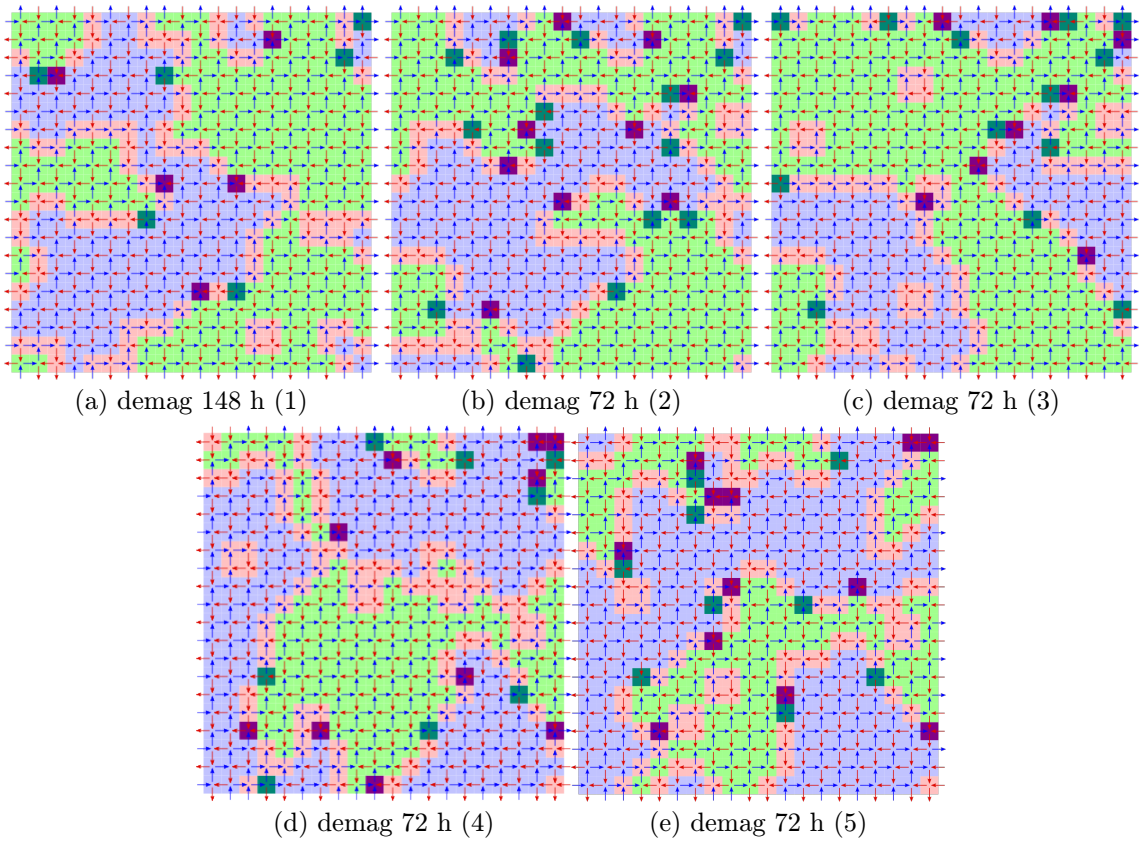

(a) demag 148 h (1) (b) demag 72 h (2) (c) demag 72 h (3)

(d) demag 72 h (4) (e) demag 72 h (5)

Fig. 4.5: Comparison of magnetic configurations measured on reference lattice ($\alpha = 45\ °$, $g_1 = 300\,\text{nm}$, dose 5) after each demagnetization protocol.

As the resulting configurations are rather consistent we can consider all demagnetization protocols equivalent. To proof this claim we state that on average the vertex populations for the reference lattice are: 74.95±0.61 %, 20.25±0.63 %, 4.80±0.58 %, 0 % for type I, II, III, IV vertices, respectively. The population of type I vertices is comparable with field demagnetized regular square lattices from previous works [15, 20, 46]. Thus we consider demagnetization protocols to be efficient in bringing the system lattices close to low-energy manifolds.

4.4.2 Captured configurations and vertex populations

For reasons that will be described and discussed later, we will now focus on d5g300 lattice set. The effect of distortion can be directly illustrated by comparing measured magnetic configurations of lattices belonging to this set (see Fig. 4.6). We can see (except for the second image), that the number of type I vertices slowly reduces and the number of type II and type III vertices gradually increase with the distortion of the lattice.

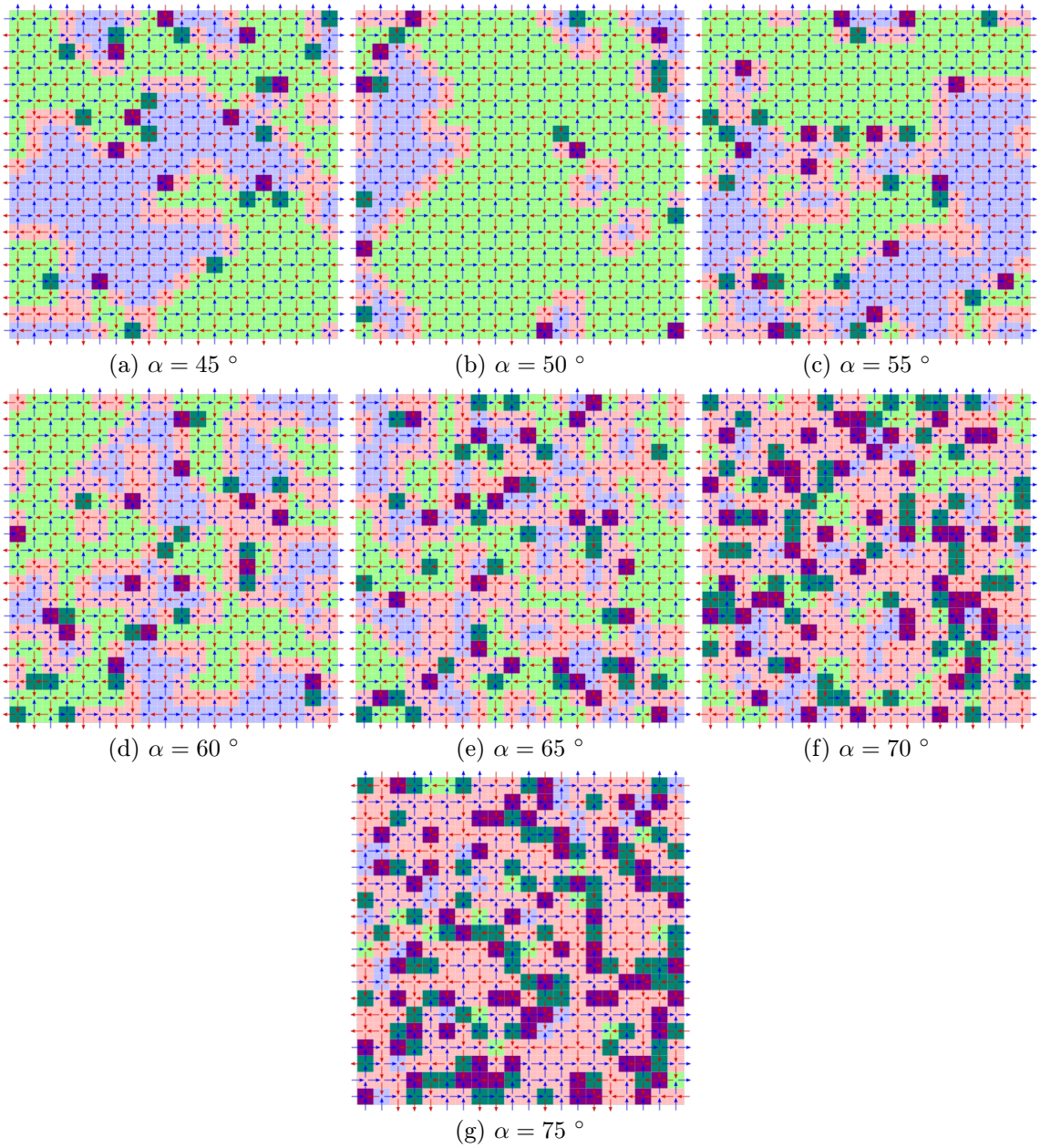

(a) $\alpha = 45$ ° (b) $\alpha = 50$ ° (c) $\alpha = 55$ °

(d) $\alpha = 60$ ° (e) $\alpha = 65$ ° (f) $\alpha = 70$ °

(g) $\alpha = 75$ °

Fig. 4.6: Magnetic configurations of d5g300 lattice set measured after 72 h demagnetization (2), selected corresponding magnetic structure factors are in Fig. 4.8

Fig. 4.7 shows how the vertex populations (averaged over 5 demagnetizations) evolve with the distortion of the lattice.

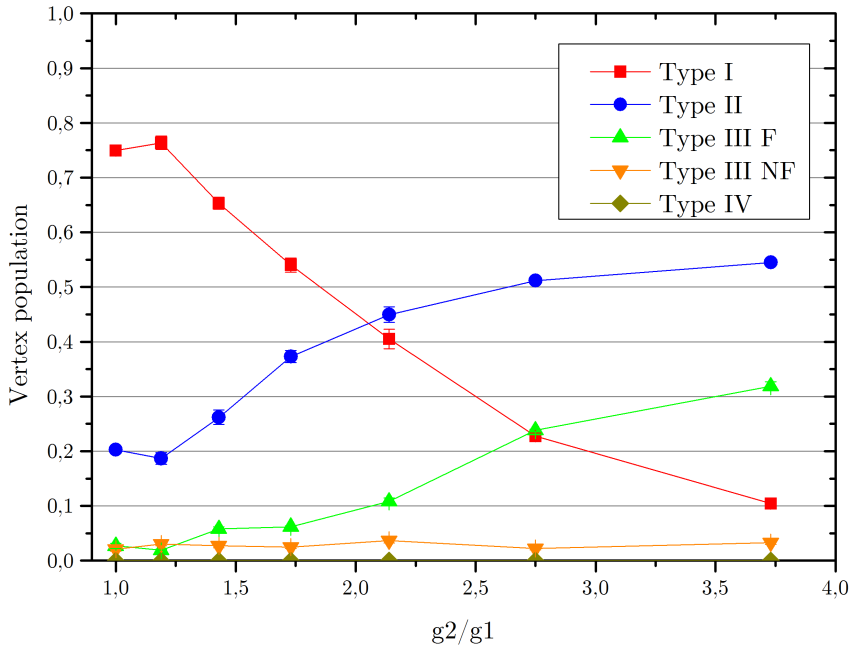

(a) Vertex populations

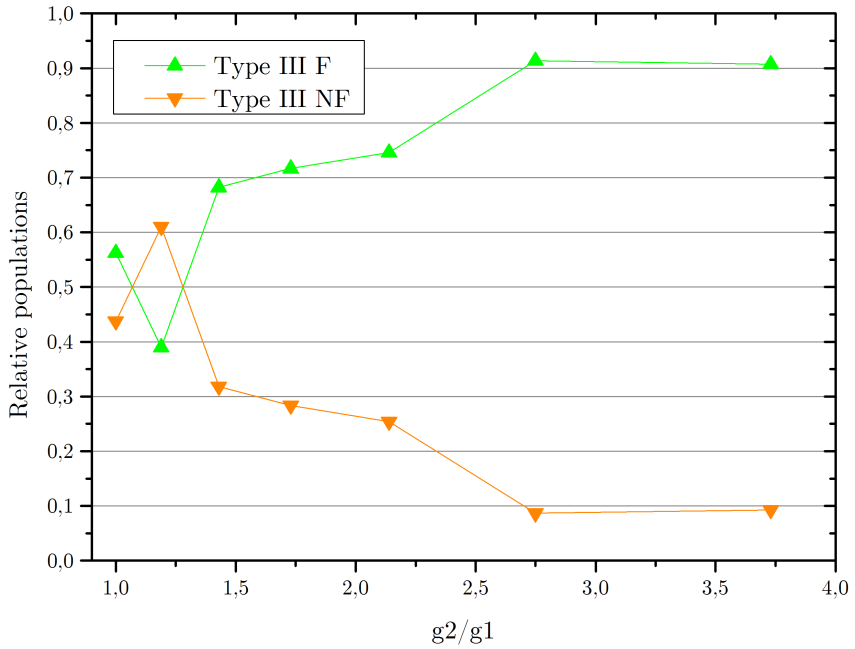

(b) Type III F/NF populations

Fig. 4.7: Vertex populations (a) and relative type III populations (b) for d5g300 lattice set averaged over 5 demagnetization protocols (resp. configurations obtained/measured after the demagnetization). Error bars represents standard error, the marking is consistent with the simulation results.

Fig. 4.7 shows remarkable consistency when compared with the simulation results

(see Fig. 4.3) and illustrates expected consequences of distortion (modification of energy levels of type I and type II, and split of type III vertices – favourable and non-favourable alignment). Based on vertex populations (resp. magnetic configurations) we can estimate what magnetic phases were captured. Here we expect AFM like ordered phase for the first lattice, liquid-like disordered phase for the sixth lattice and FM/line ordered phase for the last one. The best way to confirm this is to calculate associated magnetic structure factors (Fig. 4.8).

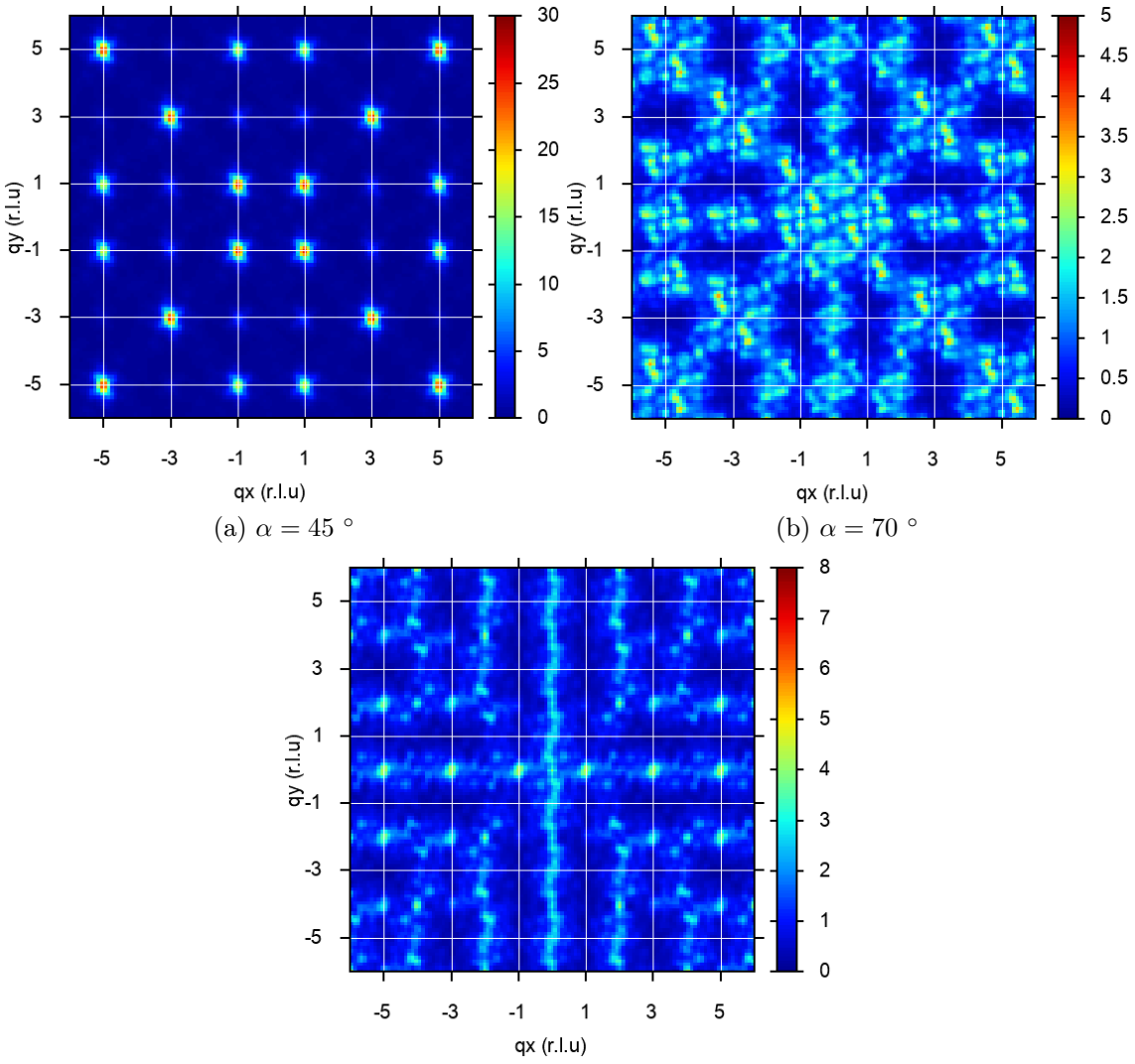

(a) $\alpha = 45$ °

(b) $\alpha = 70$ °

(c) $\alpha = 75$ °

Fig. 4.8: Magnetic structure factors for selected d5g300 lattices, corresponds to configurations showed in Fig. 4.6.

Magnetic structure factors presented in Fig. 4.8 have expected characteristic patterns (as presented in Fig. 3.13). More detailed description of captured magnetic phases (within the d5g300 lattice set) is provided in following subsections.

4.4.3 AFM phase

As expected, the AFM ground-state like configuration is captured on regular square lattice (no distortion, d5g300 $\alpha = 45\,^{\circ}$). The overall summary regarding this phase is provided in Fig. 4.9. Subfig. a) shows typical low-energy manifold of regular artificial square lattice. Big domains of type I vertices (lightblue/lightgreen) are separated by domain-walls formed mostly by type II vertices (red). Charge defects (type III vertices – darkgreen/magenta) are incorporated within these domain walls, and cannot move freely within the configuration. Subfig. b) provides a moment map of same configuration. Arrows on white background represents net vertex moment of type II vertices, which forms the domain-walls. Red squares represent closed loop configuration of four type II vertices forming a small patch. Magenta/darkgreen circles represents type III vertices, their net moment is also drawn by black arrow.

Subfig. c) shows overlay of all 5 vertex maps (for different demagnetizations – see Fig. 4.5), blue/lightred/brown squares represent type I/II/III vertices that are always at a same position. We can see that only a fraction of type II vertices (4 to be precise) and one type III vertex appear at the same place for all 5 configurations. Therefore, we can say that the forming of domain walls is not driven by lattice defects and domain walls can run through the lattice in many ways.

As the configurations (obtained after 5 demagnetization processes) do not differ substantially, the averaged (subfig. d) and individual (subfig. b) magnetic structure factor are almost the same. Only difference is that averaged one have slightly rounder Bragg peaks.

As the magnetic configuration is not perfectly ordered, the Bragg peaks in averaged MSF are less intensive and broader than for a ideal ground state (subfig. f), but placed at the same positions.

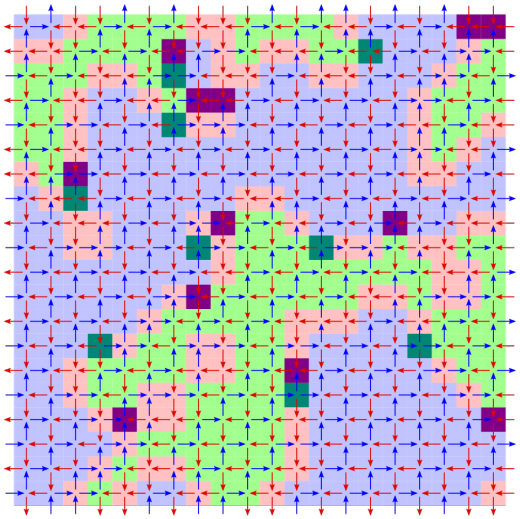

(a) Spin configuration – demag (5)

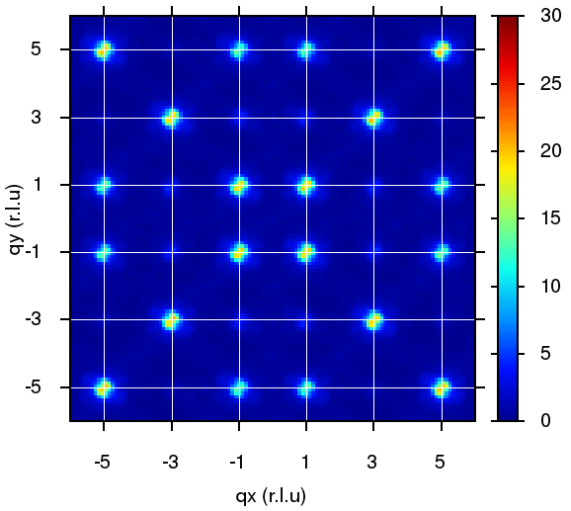

(b) Corresponding MSF to (a)

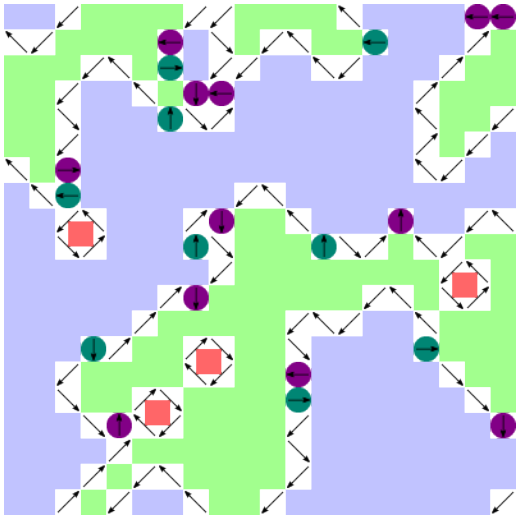

(c) Moment map of (a)

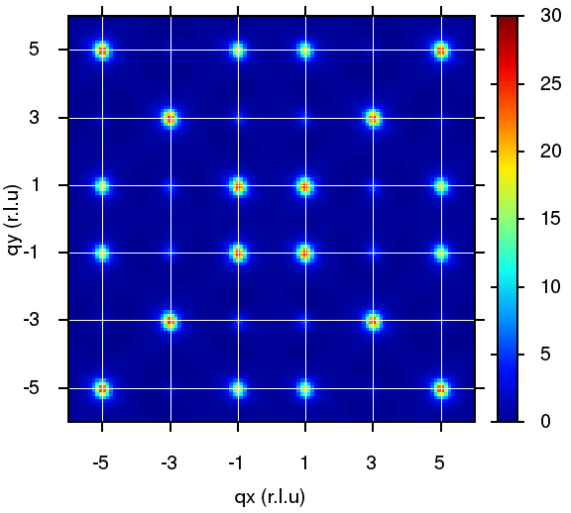

(d) Averaged MSF (5 demags)

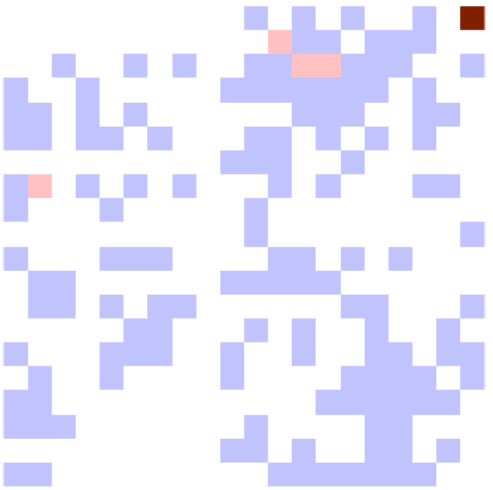

(e) Vertex map overlay (5 demags)

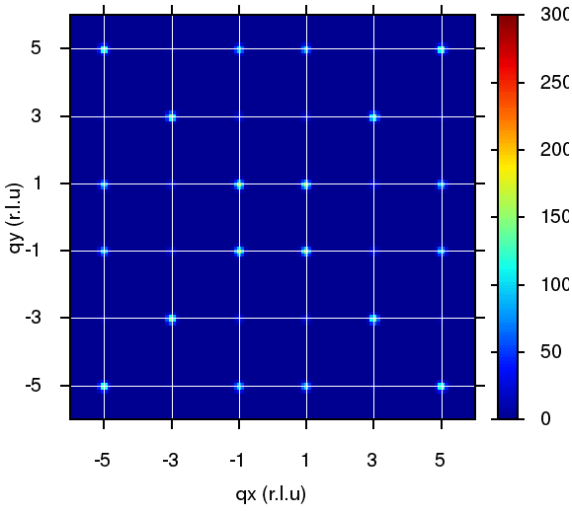

(f) Ideal MSF

Fig. 4.9: AFM phase, d5g300 $\alpha = 45$ °.

4.4.4 SL phase

Disordered spin-liquid like magnetic configuration was reached for lattice with rather significant distortion $\alpha = 70$ °, therefore the vertex populations differ substantially from an AFM ground state. Averaged populations of sixth lattice are: 22.75 %, 51.20 %, 26.05 % for type I, II and III respectively. As the distortion is significant, the type III vertices are almost all (approx. 90 %) aligned favourably (type III F).

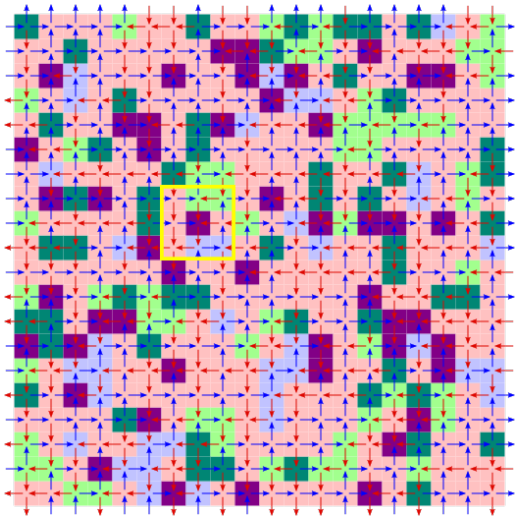

(a) Spin configuration – demag (2)

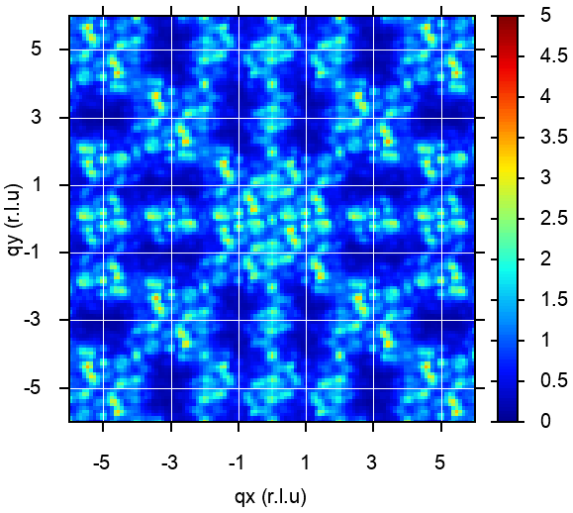

(b) Corresponding MSF to (a)

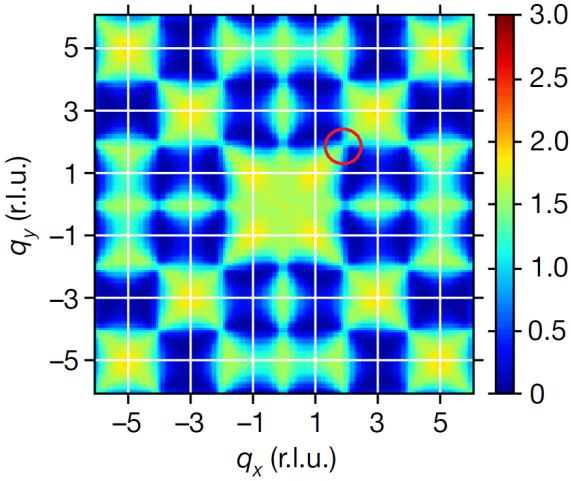

(c) Ideal MSF [20]

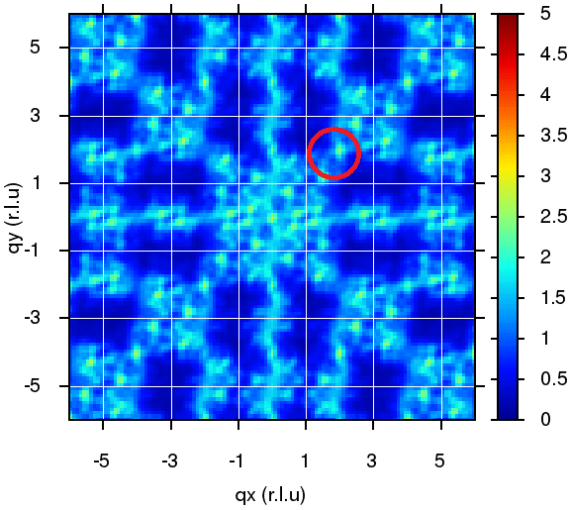

(d) Averaged MSF (4 demags)

Fig. 4.10: SL phase, d5g300 $\alpha = 70$ °.

Even thought the averaging of MSF helps to even out parts of diffused background, still the overall intensity remains slightly higher than for an ideal disordered spin-liquid phase. The vertex populations also differ from the ideal spin-liquid phase: true-degeneracy of 6 vertex model (1:2 resp. 33 % : 66 % in favour of type II vertices), both reduced approx. by 10 % (because of presence of type III vertices).

In subfig. c) and d) red circles mark pinch-points (typical features of spin-liquid phase). In d) pinch-points are much broader as their width can be directly linked with density of charged quasi-particles (type III vertices). The density of charged particles trapped within the SL phase is approx. two times larger for DSL system than in case of z-shifted system [28].

In case of disordered spin-liquid phase the charged quasi-particles are considered deconfined and they can move freely within the system (they are described as magnetic monopoles that interact via Coulomb potential) [18]. In case of DSL system their freedom of movement is constrained by the lattice geometry, as they must align their net moment with closer gap (i.e. they must rotate their net magnetic moment by 90° when moving to neighbouring vertex point). It is even possible that with a certain orientation of uncharged neighbours, monopole can get trapped by them (see Fig. 4.11).

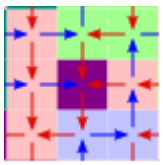

Fig. 4.11: Example of monopole trapped by type I and type II vertices, extracted from Fig. 4.10a – marked by yellow frame.

4.4.5 FM/line phase

It is expected that distortion higher than α_c will lead to FM/line phase, seventh lattice ($\alpha = 75°$). This phase is prevailed by type II vertices. As the DSL geometry enables all 4 possible type II configurations, they tend to create polarized line arrangement (see Fig.3.13c). These lines are interrupted and influenced by type I and type III vertices, which can lead to characteristic lines in background of MSF pattern [30]. The overall summary regarding this phase is provided in Fig. 4.12. As there are recognizable Bragg peaks present within the magnetic diffraction pattern (Fig. 4.12d), the phase can be considered as FM/line ordered phase.

Again type III vertices are present, they even significantly prevails over type I vertices. As the lattice is highly distorted, the type III vertices must align with the lattice geometry (type III F). This in fact limits the length (and ordering) of lines, as it is likely that the line will be broken by the perpendicularly aligned type III vertex (see Fig. 4.12a). Therefore the type III vertices bring more disorder to the system. If we look at the high-distortion limit (not-fabricated) in simulations (Fig. 4.3, 8 data point) the new disordered phase of type II and type III F (ratio 1:1) may

be expected/reached.

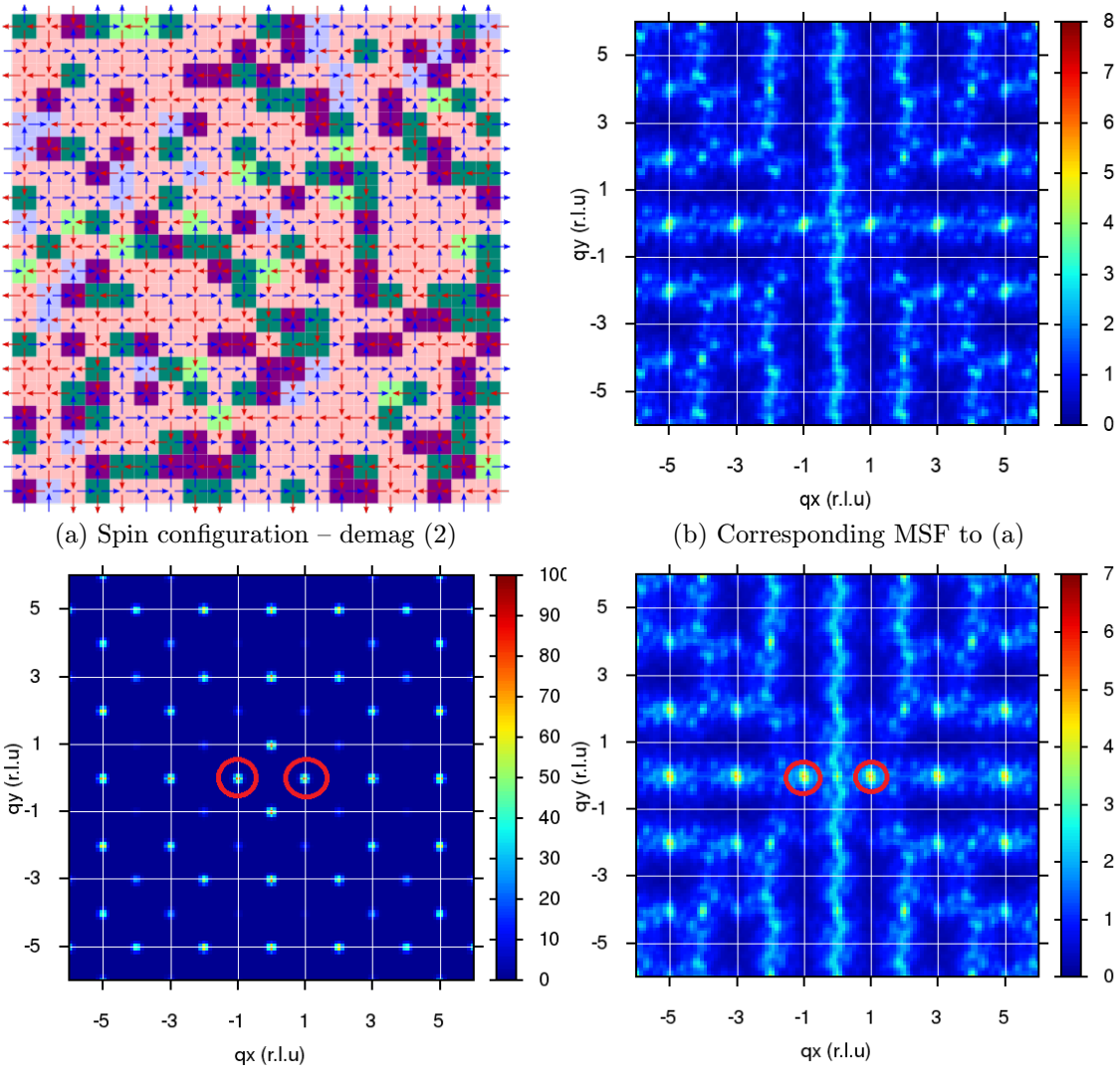

(a) Spin configuration – demag (2)

(b) Corresponding MSF to (a)

(c) Ideal MSF – line phase

(d) Averaged MSF (5 demags)

Fig. 4.12: FM/line phase, d5g300 $\alpha = 75$ °.

4.4.6 Influence of exposure dose

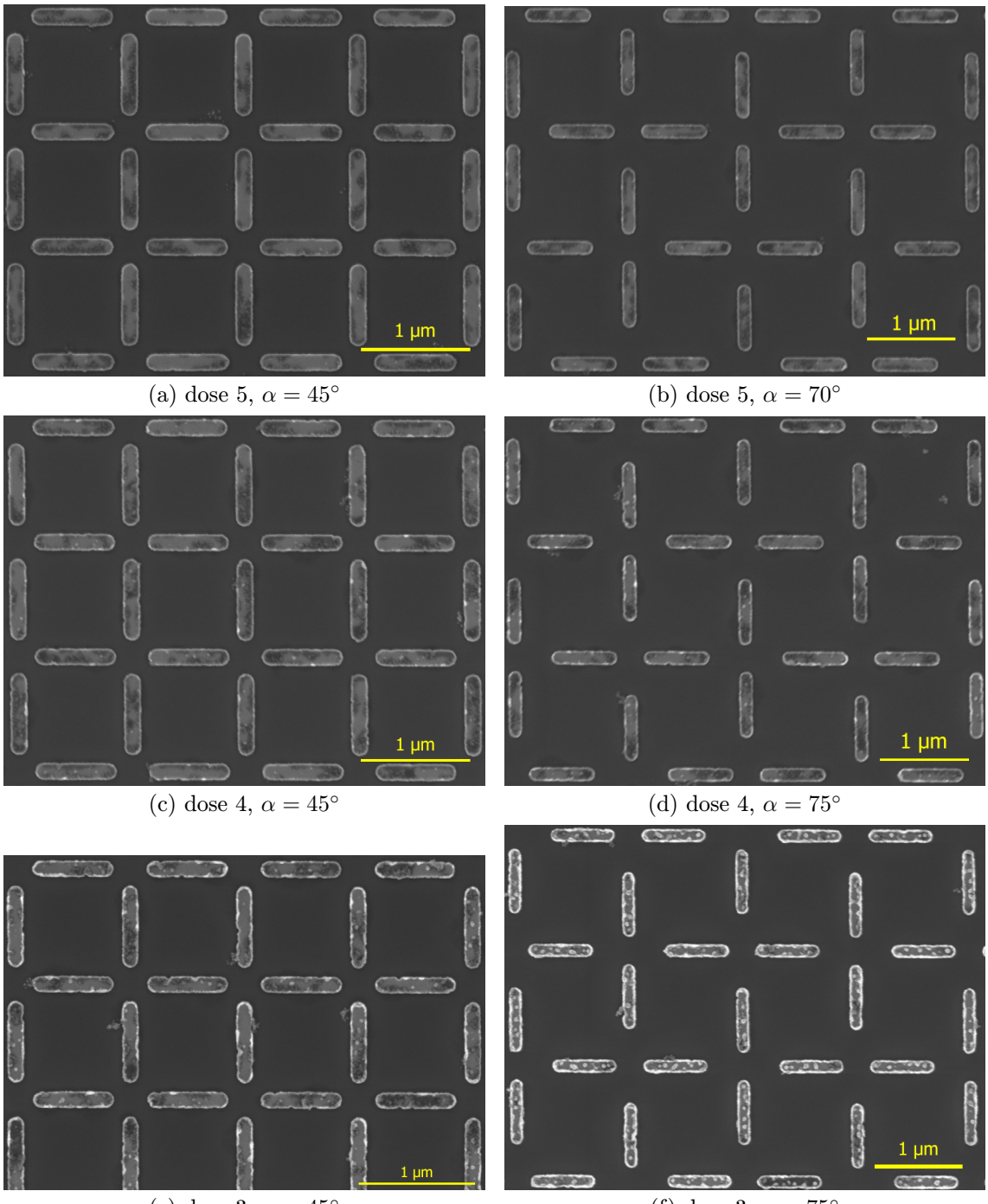

(a) dose 5, $\alpha = 45°$

(b) dose 5, $\alpha = 70°$

(c) dose 4, $\alpha = 45°$

(d) dose 4, $\alpha = 75°$

(e) dose 3, $\alpha = 45°$

(f) dose 3, $\alpha = 75°$

Fig. 4.13: SEM images of fabricated lattices of artificial spin systems with $g_1 = 300$ nm for different exposure doses.

Fig. 4.13 shows that the quality of fabrication degrades with lower dose – magnets starts to be rougher (from top view) and for dose 3 it looks like there are vertical

residues from the lift-off (ears), some of them broke off and lie on top of the magnets.

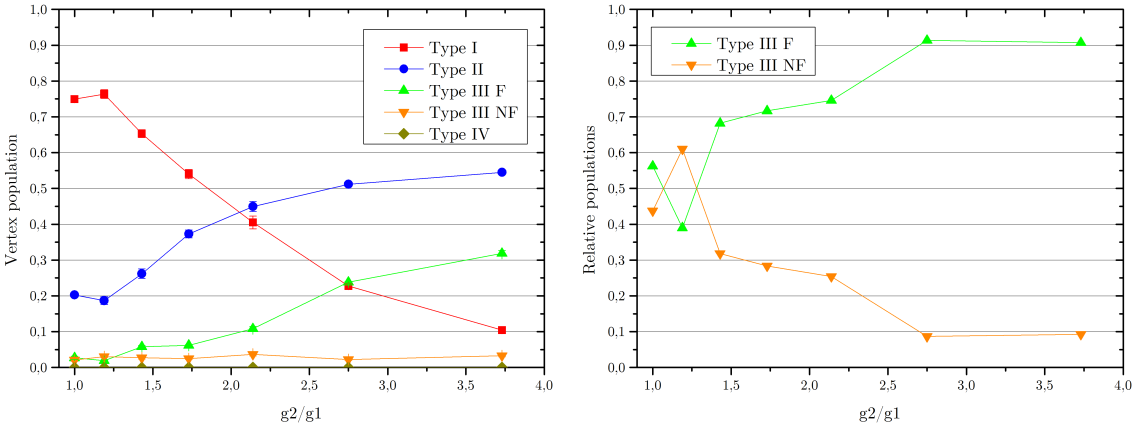

(a) Vertex populations, dose 5

(b) Type III F/NF, dose 5

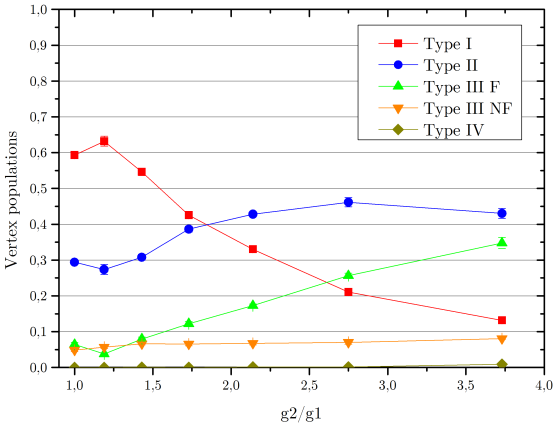

(c) Vertex populations, dose 4

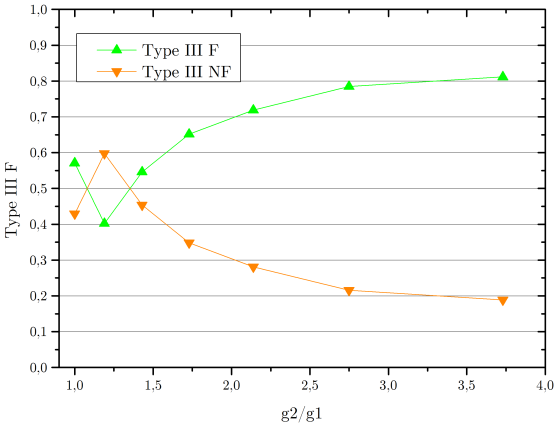

(d) Type III F/NF, dose 4

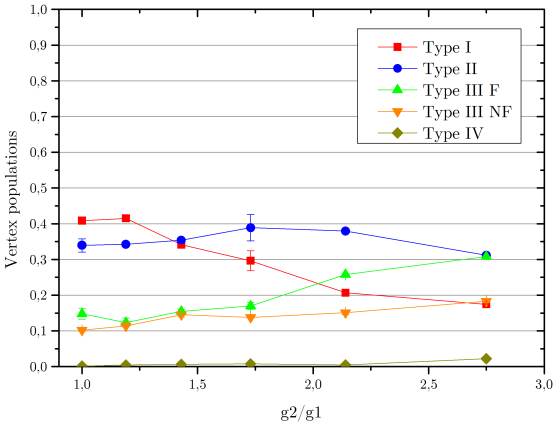

(e) Type III F/NF, dose 3

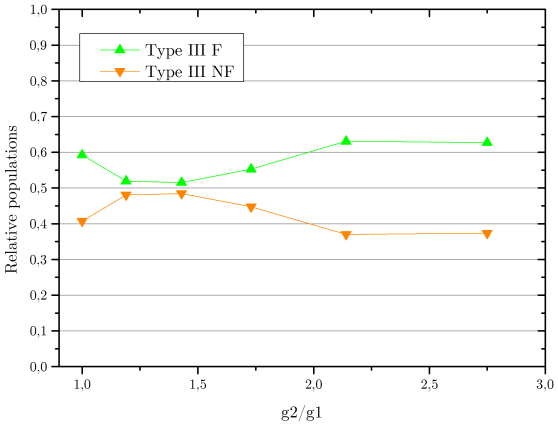

(f) dose 3, $\alpha = 75°$

Fig. 4.14: Averaged vertex populations of artificial spin systems with $g_1 = 300$ nm for different exposure doses. Dose 5 and 4 averaged over 5 demags, dose 3 averaged over 2 demags. Error bars represents standard error, the marking is consistent with the simulation results.

Fig. 4.14 shows how the quality of fabrication directly influences the vertex populations of artificial spin systems. Higher the dose, the better the system performs. Similar trend can be recognized from MSF as with lower dose all the patterns are more diffused.

4.4.7 Influence of gap size

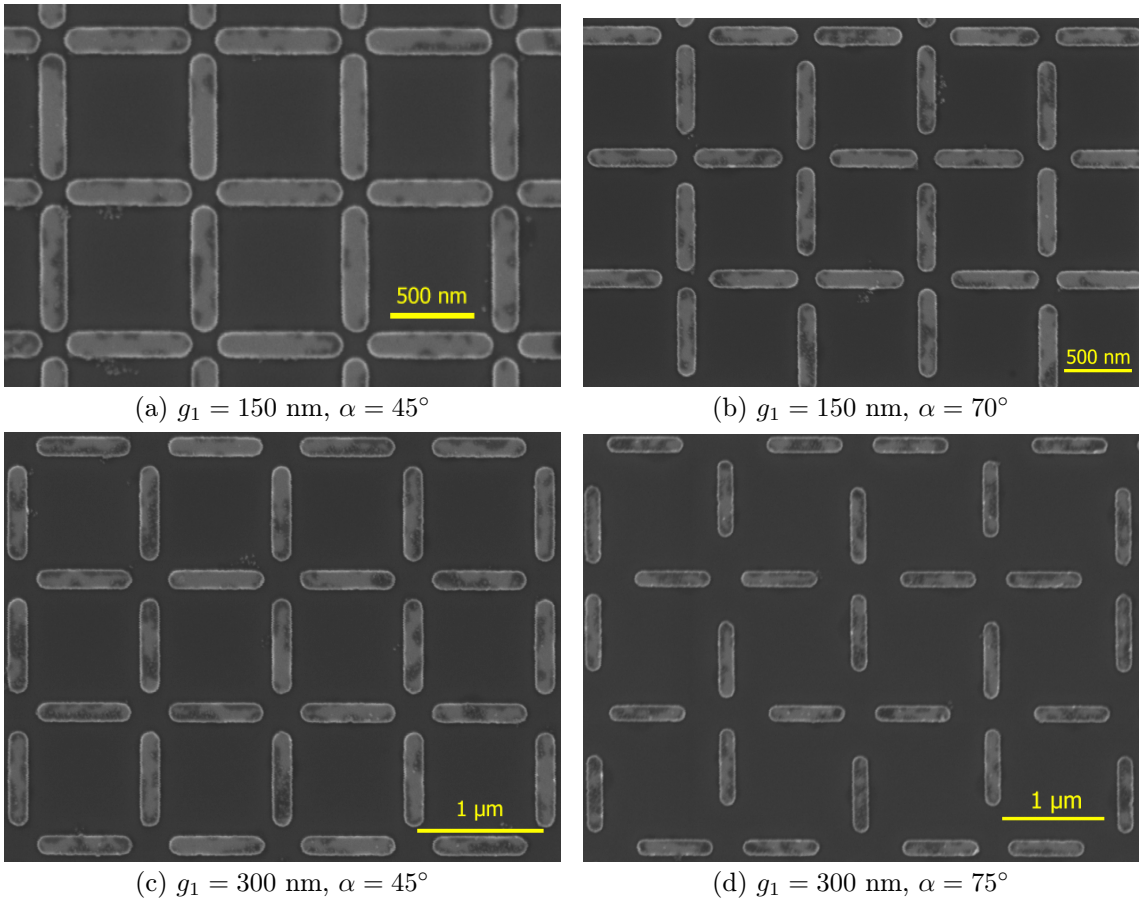

(a) $g_1 = 150$ nm, $\alpha = 45°$

(b) $g_1 = 150$ nm, $\alpha = 70°$

(c) $g_1 = 300$ nm, $\alpha = 45°$

(d) $g_1 = 300$ nm, $\alpha = 75°$

Fig. 4.15: SEM images of fabricated lattices of artificial spin systems with dose 5 for different base gap sizes.

Fig. 4.15 shows that lattices with both base gaps (g150, g300) exhibits high-quality fabrication (dose 5). Therefore one would expect that with g150 set it should be possible to reach closer to low-energy configuration for reference lattice ($\alpha = 45°$). This is also supported by the simulations as there is bigger energy difference between type I and type II vertices for smaller gap (see Fig. 4.4 and 4.3).

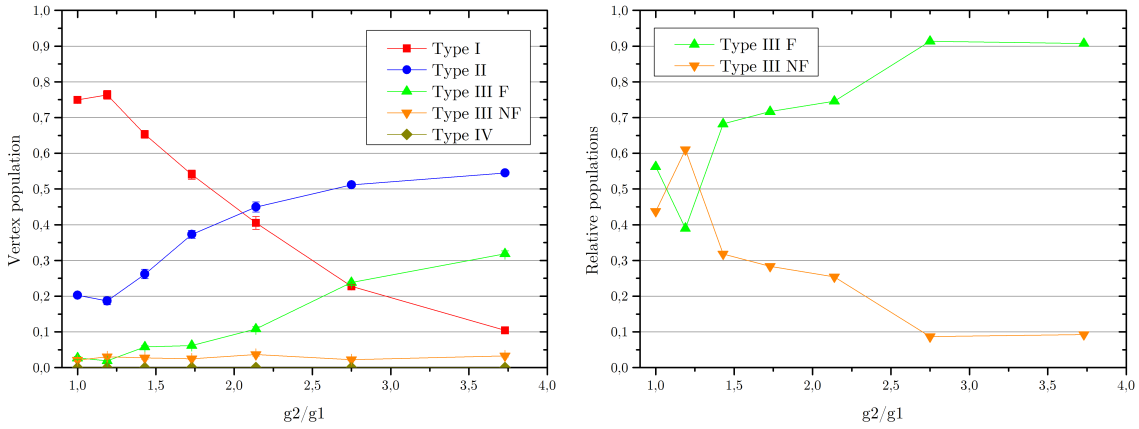

(a) Vertex populations, g300

(b) Type III F/NF, g300

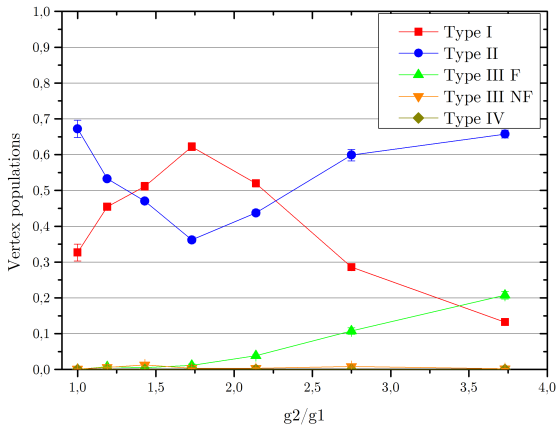

(c) Vertex populations, g150

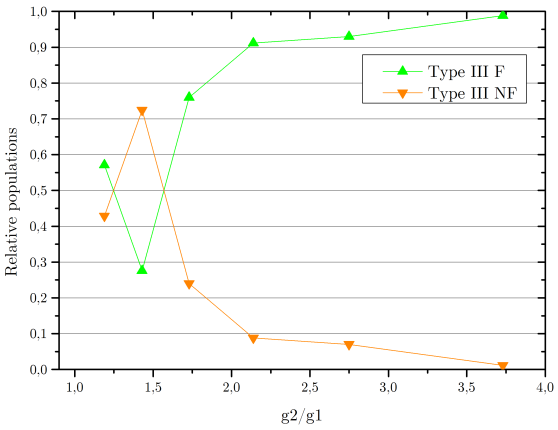

(d) Type III F/NF, g150

Fig. 4.16: Averaged vertex populations of artificial spin systems with $g_1 = 300$ nm and $g_1 = 150$ nm for exposure dose 5. g300 averaged over 5 demags, g150 averaged over 4 demags. Error bars represents standard error, the marking is consistent with the simulation results.

Fig. 4.16 reveals interesting trend for g150 lattices, as first 3 data points have completely unexpected positions. From the fourth point the system behaves consistently with the g300 set.

5 CONCLUSION

Since their introduction in 2006, artificial magnetic spin systems became of a great interest, as they enable exploring of low-energy unconventional magnetic phases directly in real space. Firstly, their research was driven by efforts to create a model systems that would mimic the properties of natural frustrated compounds. As they provide great tunability through the fabrication methods, they quickly became a tool for inducing targeted phenomenon or property of the system.

In this work, we present a novel spin system geometry (acronym DSL) which, enables experimental scanning through the phase diagram of the seminal ice-type model (6 vertex model), by tuning a single geometrical parameter of its design. The proposed geometry was experimentally realized utilizing the conventional lift--off technique combined with electron beam lithography and the system lattices were brought to theirs low-energy configurations by field demagnetization protocol. Magnetic configurations (magnetic phases) were than measured by magnetic force microscopy.

The results provide strong evidence that distinct magnetic phases were reached and that the tuning of the design is effective. With the appropriate tuning we were able to observe signatures of disordered spin-liquid phase, which is in fact experimental realization of well-known ice model. Our results also reveal that charged quasi-particles (magnetic monopoles) can be trapped within this liquid-like magnetic phase. In case of our system their dynamics seems to be different (than in previous experimental studies), as new constraint regarding their freedom of movement emerges from the lattice geometry. As the tuning affects both, density of these quasi-particles and resulting magnetic phase, we cannot obtain spin-liquid phase with various densities. Therefore, our lattice cannot be used to test the theoretical proposal of spin fragmentation in a direct manner.

BIBLIOGRAPHY

[1] Pauling, L. The Structure and Entropy of Ice and of Other Crystals with Some Randomness of Atomic Arrangement. *Journal Of The American Chemical Society*, 57(12), 2680-2684, 1935. https://doi.org/10.1021/ja01315a102.

[2] Giauque, W. F., Ashley, M. F. Molecular Rotation in Ice at 10°K. Free Energy of Formation and Entropy of Water. *Physical Review*, 43(1), 81-82, 1933. https://doi.org/10.1103/PhysRev.43.81.2.

[3] Bernal, J. D., Fowler, R. H. A Theory of Water and Ionic Solution, with Particular Reference to Hydrogen and Hydroxyl Ions. The Journal Of Chemical Physics, 1(8), 515-548, 1933. https://doi.org/10.1063/1.1749327.

[4] Bramwell, S. T., Gingras, M. J. P., Holdsworth, P. C. W. SPIN ICE. *Frustrated Spin Systems*, 383-474, 2013. https://doi.org/10.1142/9789814440745_0007.

[5] Anderson, P. W. Ordering and Antiferromagnetism in Ferrites. *Physical Review*, 102(4), 1008-10131 1956. https://doi.org/10.1103/PhysRev.102.1008.

[6] Wannier, G. H. Antiferromagnetism. The Triangular Ising Net. *Physical Review*, 79(2), 357-364, 1950. https://doi.org/10.1103/PhysRev.79.357.

[7] Lieb, E. H. Exact Solution of the Problem of the Entropy of Two-Dimensional Ice. *Physical Review Letters*, 18(17), 692-694, 1967. https://doi.org/10.1103/PhysRevLett.18.692.

[8] Lieb, E. H. Exact Solution of the Two-Dimensional Slater KDP Model of a Ferroelectric. *Physical Review Letters*, 19(3), 108-110, 1967. https://doi.org/10.1103/PhysRevLett.19.108.

[9] Lieb, E. H. Exact Solution of the F Model of An Antiferroelectric. Physical Review Letters, 18(24), 1046-1048, 1967. https://doi.org/10.1103/PhysRevLett.18.1046.

[10] Slater, J. C. Theory of the Transition in KH 2 PO 4. *The Journal Of Chemical Physics*, 9(1), 16-33, 1941. https://doi.org/10.1063/1.1750821.

[11] Rys, F. U̇ber ein zweidimensionales klassisches Konfigurationsmodell. *Helvetica Physica Acta*, 36, 537-559, (1963). https://doi.org/http://doi.org/10.5169/seals-113387.

[12] Lieb, E. H. Two-Dimensional Ferroelectric Models. *Condensed Matter Physics And Exactly Soluble Models*, 473-474, (2004). https://doi.org/10.1007/978-3-662-06390-3_30.

[13] Baxter, R. J. Exactly solved models in statistical mechanics [Online]. New York: Academic Press, 1982. Retrieved from: https://physics.anu.edu.au/theophys/_files/Exactly.pdf. Accessed: 2019-04-05.

[14] Harris, M. J., Bramwell, S. T., McMorrow, D. F., Zeiske, T., Godfrey, K. W. Geometrical Frustration in the Ferromagnetic Pyrochlore Ho 2 Ti 2 O 7. Physical Review Letters, 79(13), 2554-2557, 1997. https://doi.org/10.1103/PhysRevLett.79.2554.

[15] Wang, R. F., Nisoli, C., Freitas, R. S., Li, J., McConville, W., Cooley, B. J., et al. Artificial 'spin ice' in a geometrically frustrated lattice of nanoscale ferromagnetic islands. *Nature*, 439(7074), 303-306, 2006. https://doi.org/10.1038/nature04447.

[16] Nisoli, C., Moessner, R., Schiffer, P. (2013). Colloquium: Artificial spin ice: Designing and imaging magnetic frustration. *Reviews Of Modern Physics*, 85(4), 1473-1490. https://doi.org/10.1103/RevModPhys.85.1473.

[17] Nisoli, C. Topology by Design in Magnetic Nano-materials: Artificial Spin Ice. *The Role Of Topology In Materials*, 85-112, 2018. https://doi.org/10.1007/978-3-319-76596-9_4.

[18] Rougemaille, N., Canals, B. Cooperative magnetic phenomena in artificial spin systems: spin liquids, Coulomb phase and fragmentation of magnetism – a colloquium. *The European Physical Journal B*, 92(3), 2019. https://doi.org/10.1140/epjb/e2018-90346-7.

[19] Anderson, P. W. The concept of frustration in spin glasses. *Journal Of The Less Common Metals*, 62, 291-294, 1978. https://doi.org/10.1016/0022-5088(78)90040-1.

[20] Perrin, Y. *Réseaux artificiels à frustration géométrique.* Dissertation thesis, Université Grenoble Alpes, 2016. Retrieved from: https://tel.archives-ouvertes.fr/tel-01528873v2. Accessed: 2019-03-18.

[21] Schánilec, V. *Magnetic spin ice states in artifcial magnetic frustrated systems.* Diploma thesis, Brno University of Technology, 2018. Retrieved from: https://www.vutbr.cz/studenti/zav-prace/detail/109717. Accessed: 2019-03-15.

[22] Giauque, W. F., Stout, J. W. The Entropy of Water and the Third Law of Thermodynamics. The Heat Capacity of Ice from 15 to 273°K. *Journal Of The American Chemical Society*, 58(7), 1144-1150, 1936. https://doi.org/10.1021/ja01298a023.

[23] Levis, D. *Two-dimensional Spin Ice and the Sixteen-Vertex Model*. Dissertation thesis, Université Pierre et Marie Curie, 2012. Retrieved from: https://tel.archives-ouvertes.fr/tel-00763350. Accessed: 2019-03-18.

[24] Ramirez, A. P., Hayashi, A., Cava, R. J., Siddharthan, R., Shastry, B. S. Zero--point entropy in 'spin ice'. *Nature*, 399(6734), 333-335, 1999. https://doi.org/10.1038/20619.

[25] Moessner, R., Tchernyshyov, O., Sondhi, S. L. Planar Pyrochlore, Quantum Ice and Sliding Ice. *Journal Of Statistical Physics*, 116(1-4), 755-772, 2004. https://doi.org/10.1023/B:JOSS.0000037247.54022.62.

[26] Tanaka, M., Saitoh, E., Miyajima, H., Yamaoka, T., Iye, Y. Magnetic interactions in a ferromagnetic honeycomb nanoscale network. *Physical Review B*, 73(5), 2006. https://doi.org/10.1103/PhysRevB.73.052411.

[27] Möller, G., Moessner, R. Artificial Square Ice and Related Dipolar Nanoarrays. *Physical Review Letters*, 96(23), 2006. https://doi.org/10.1103/PhysRevLett.96.237202.

[28] Perrin, Y., Canals, B., Rougemaille, N. Extensive degeneracy, Coulomb phase and magnetic monopoles in artificial square ice. *Nature*, 540(7633), 410-413, 2016. https://doi.org/10.1038/nature20155.

[29] Schánilec, V., Yann, P., Le Denmat, S., Canals, B., Rougemaille, N. Artificial vertex systems by design. *Arxiv.org*, arXiv:1902.00452, 1-21, 2019. Retrieved from: https://arxiv.org/abs/1902.00452.

[30] Östman, E., Stopfel, H., Chioar, I. -A., Arnalds, U. B., Stein, A., Kapaklis, V., Hjörvarsson, B. Interaction modifiers in artificial spin ices. *Nature Physics*, 14(4), 375-379, 2018. https://doi.org/10.1038/s41567-017-0027-2.

[31] Ribeiro, I. R. B., Nascimento, F. S., Ferreira, S. O., Moura-Melo, W. A., Costa, C. A. R., Borme, J., et al. Realization of Rectangular Artificial Spin Ice and Direct Observation of High Energy Topology. *Scientific Reports*, 7(1), 2017. https://doi.org/10.1038/s41598-017-14421-w.

[32] Castelnovo, C., Moessner, R., Sondhi, S. L. Magnetic monopoles in spin ice. *Nature*, 451(7174), 42-45, 2008. https://doi.org/10.1038/nature06433.

[33] Brooks-Bartlett, M. E., Banks, S. T., Jaubert, L. D. C., Harman-Clarke, A., Holdsworth, P. C. W. Magnetic-Moment Fragmentation and Monopole Crystallization. *Physical Review X*, 4(1), 2014. https://doi.org/10.1103/PhysRevX.4.011007.

[34] Donahue, M., Porter, D. Interagency Report *NISTIR 6376*, National Institute of Standards and Technology, Gaithersburg, MD, 1999. Available at: http://math.nist.gov/oommf. Accessed: 2019-05-08.

[35] Vansteenkiste, A., Leliaert, J., Dvornik, M., Helsen, M., Garcia-Sanchez, F., Van Waeyenberge, B. The design and verification of MuMax3. *Aip Advances*, 4(10), 2014. https://doi.org/10.1063/1.4899186.

[36] Nguyen, V. -D., Perrin, Y., Le Denmat, S., Canals, B., Rougemaille, N. Competing interactions in artificial spin chains. *Physical Review B*, 96(1), 2017. https://doi.org/10.1103/PhysRevB.96.014402.

[37] Chen, Y. Nanofabrication by electron beam lithography and its applications: A review. *Microelectronic Engineering*, 135, 57-72, 2015. https://doi.org/10.1016/j.mee.2015.02.042.

[38] Broers, A. N. Resolution limits for electron-beam lithography. *Ibm Journal Of Research And Development*, 32(4), 502-513, 1988. https://doi.org/10.1147/rd.324.0502

[39] Hu, W. (W.), Sarveswaran, K., Lieberman, M., Bernstein, G. H. Sub-10 nm electron beam lithography using cold development of poly(methylmethacrylate). *Journal Of Vacuum Science & Technology B: Microelectronics And Nanometer Structures Processing, Measurement, And Phenomena*, 22(4), 2004. https://doi.org/10.1116/1.1763897.

[40] Singh, J., Wolfe, D. E. Review Nano and macro-structured component fabrication by electron beam-physical vapor deposition (EB-PVD). *Journal Of Materials Science*, 40(1), 1-26, 2005. https://doi.org/10.1007/s10853-005-5682-5.

[41] Wajid, A. On the accuracy of the quartz-crystal microbalance (QCM) in thin-film depositions. *Sensors And Actuators A: Physical*, 63(1), 41-46, 1997. https://doi.org/10.1016/S0924-4247(97)80427-X.

[42] Ustinov, A. I., Demchenkov, S. A., Polischuk, S. S., Telychko, V. A. Effect of deposition conditions of Fe100−xNix (30¡x¡40) condensates on their structure.

Surface And Coatings Technology, 251, 247-253, 2014. https://doi.org/10.1016/j.surfcoat.2014.04.033.

[43] Wang, R. F., Li, J., McConville, W., Nisoli, C., Ke, X., Freeland, J. W., et al. Demagnetization protocols for frustrated interacting nanomagnet arrays. *Journal Of Applied Physics*, 101(9), 2007. https://doi.org/10.1063/1.2712528.

[44] Ke, X., Li, J., Nisoli, C., Lammert, P. E., McConville, W., Wang, R. F., et al. Energy Minimization and ac Demagnetization in a Nanomagnet Array. *Physical Review Letters*, 101(3), 2008. https://doi.org/10.1103/PhysRevLett.101.037205.

[45] Budrikis, Z., Politi, P., Stamps, R. L. Diversity Enabling Equilibration: Disorder and the Ground State in Artificial Spin Ice. *Physical Review Letters*, 107(21), 2011. https://doi.org/10.1103/PhysRevLett.107.217204.

[46] Morgan, J. P., Bellew, A., Stein, A., Langridge, S., Marrows, C. H. Linear field demagnetization of artificial magnetic square ice. *Frontiers In Physics*, 1, 2013. https://doi.org/10.3389/fphy.2013.00028.

[47] Farhan, A., Derlet, P. M., Kleibert, A., Balan, A., Chopdekar, R. V., Wyss, M., et al. Direct Observation of Thermal Relaxation in Artificial Spin Ice. *Physical Review Letters*, 111(5), 2013. https://doi.org/10.1103/PhysRevLett.111.057204.

[48] Kapaklis, V., Arnalds, U. B., Farhan, A., Chopdekar, R. V., Balan, A., Scholl, A., et al. Thermal fluctuations in artificial spin ice. *Nature Nanotechnology*, 9(7), 514-519, 2014. https://doi.org/10.1038/nnano.2014.104.

[49] Binnig, G., Quate, C. F., Gerber, C. Atomic Force Microscope. *Physical Review Letters*, 56(9), 930-933, 1986. https://doi.org/10.1103/PhysRevLett.56.930.

[50] Martin, Y., Wickramasinghe, H. K. Magnetic imaging by "force microscopy" with 1000 Å resolution. *Applied Physics Letters*, 50(20), 1455-1457, 1987. https://doi.org/10.1063/1.97800.

[51] Mironov, V. L. Fundamentals of scanning probe microscopy [Online]. Nizhniy Novgorod: The Russian Academy of Sciences – Institute for Physics of Microstructures, 2004. Retrieved from https://www.weizmann.ac.il/ChemicalResearchSupport/sites/ChemicalResearchSupport/files/uploads/spm_fundamentals_mironov_book_en.pdf. Accessed: 2019-05-22.

[52] Kazakova, O., Puttock, R., Barton, C., Corte-León, H., Jaafar, M., Neu, V., Asenjo, A. Frontiers of magnetic force microscopy. *Journal Of Applied Physics*, 125(6), 2019. https://doi.org/10.1063/1.5050712.

[53] Nečas, D., Klapetek, P. Gwyddion: an open-source software for SPM data analysis. *Open Physics*, 10(1), 2012. https://doi.org/10.2478/s11534-011-0096-2.

LIST OF APPENDICES

A Micromagnetic simulations **79**
A.1 Example of **MuMax^3** input code 79

B Fabrication **81**
B.1 Fabrication process details 81

A MICROMAGNETIC SIMULATIONS

A.1 Example of MuMax^3 input code

```
//Simulation world parameters
Nx := 2048;
Ny := 2048;
Nz := 1;

sizeX := 2048e-9;
sizeY := 2048e-9;
sizeZ := 5e-9;

SetGridSize(Nx, Ny, Nz);
SetCellSize(sizeX/Nx, sizeY/Ny, sizeZ/Nz);

//Geometrical parameters
w:=150e-9;
l:=300e-9;
r:=75e-9;
gx:=150e-9;
gy:=322e-9; //this changes
k:=0;
bc:=50e-9;

//Simulation parameters
smu:=8;
EdgeSmooth = smu;
stime:=5e-9;
snapshotformat = "png"

//Material parameters
//permalloy
      Msat  = 800e3;
      Aex   = 10e-12;
      alpha = 0.5;

//Table settings
tableaddvar(smu, "Smooth", " ");
tableaddvar(stime, "simulation time", "s");
tableaddvar(gy, "gap y", "nm");
tableadd(E_exch);
tableadd(E_demag);
tableadd(E_total);

//Geometry load
setgeom ( imageShape("g150_k5.png") );    //geometry defined by BW bitmap
saveas(geom, "imageShape");

//Simulation

      defregion(1, rect(l-bc,w).transl(((1/2)*(l-bc)+r+((1/2)*gx)),0,0));
      defregion(2, rect(l-bc,w).transl(-((1/2)*(l-bc)+r+((1/2)*gx)),0,0));
      defregion(3, rect(w,l-bc).transl(0,((1/2)*(l-bc)+r+((1/2)*gy)),0));
      defregion(4, rect(w,l-bc).transl(0,-((1/2)*(l-bc)+r+((1/2)*gy)),0));

      defregion(5, rect(bc,w).transl(((1/2)*bc+(l-bc)+r+((1/2)*gx)),0,0));
      defregion(6, rect(bc,w).transl(-((1/2)*bc+(l-bc)+r+((1/2)*gx)),0,0));
      defregion(7, rect(w,bc).transl(0,((1/2)*bc+(l-bc)+r+((1/2)*gy)),0));
      defregion(8, rect(w,bc).transl(0,-((1/2)*bc+(l-bc)+r+((1/2)*gy)),0));

      //save(regions);

      //Vertex simulation
      m.setRegion(1, uniform(1, 0, 0));          //right wing
      m.setRegion(2, uniform(1, 0, 0));          //left wing
      m.setRegion(3, uniform(0, 1, 0));          //up wing
      m.setRegion(4, uniform(0, 1, 0));          //down wing

      m.setRegion(5, uniform(1, 0, 0));          //right wing BC
      m.setRegion(6, uniform(1, 0, 0));          //left wing BC
      m.setRegion(7, uniform(0, 1, 0));          //up wing BC
      m.setRegion(8, uniform(0, 1, 0));          //down wing BC

      //Freeze magnetization at the boundaries
      frozenspins.setRegion(5, 1)
```

```
frozenspins.setRegion(6, 1)
frozenspins.setRegion(7, 1)
frozenspins.setRegion(8, 1)

MFMLift=80e-9;

snapshot(m);
snapshot(MFM);
relax();
run(stime);
snapshot(m);
snapshot(MFM);
tablesave();
```

B FABRICATION

B.1 Fabrication process details

1. **Resist preparation**
   - Substrate: p-doped Si (100) wafer (thickness: 275 μm)
   - Resist: Allresist AR-P 679.04 (PMMA, 950 K, 4 % solids content, ethyl--lactate solvent)
   - Technique: spin coating (4000 RPM, $t = 60$ s)
   - Soft bake: hot plate (180° C, $t = 5$ min)
   - Final thickness: approx. 160 nm (measured via optical profilometer)
2. **E-beam exposure**
   - Device: SEM Zeiss Leo 1530 (with lithography kit – Raith ELPHY Plus)
   - Primary beam energy: 20 keV
   - Beam aperture: 7.5 μm
   - Beam current: 10 – 20 pA (at sample)
   - Exposure dose (nominal): 300 μC/cm^2
   - Stamp size: 5.2 x 5.2 nm
3. **Development**
   (a) First bath: (1:2) MIBK:IPA, $t = 30$ s
   (b) Second bath: IPA, $t = 60$ s
   (c) Drying by nitrogen
4. **Deposition**
   - Technique: EBPVD
   - Material: permalloy ($Ni_{80}Fe_{20}$), $t = 25\,\text{nm}$
   - Capping layer: Al, $t = 3\,\text{nm}$
   - Chamber pressure: $p = 1 \times 10^{-5}\,\text{mbar}$
   - Deposition rate: 1 Å/s
5. **Lift-off**
   (a) Lift-off bath: Remover PG (based on NMP), heated to 80 °C, $t = 60$ min
   (b) Ultrasonic treatment (approx. 10 s, low power)
   (c) Cleaning bath: IPA
   (d) Drying by nitrogen